High-fidelity CFD Validation and Assessment of Ducted Propellers for Aircraft Propulsion

Tao Zhang

PhD student,

CFD Laboratory, School of Engineering, University of Glasgow

Scotland, United Kingdom

George N. Barakos

Professor, MVFS, SMAIAA, FRAeS,

CFD Laboratory, School of Engineering, University of Glasgow,

Scotland, United Kingdom

Abstract

This paper presents validation and assessment of ducted propellers for aircraft propulsion. Numerical methods and simulation strategies are put forward, including steady/unsteady high-fidelity CFD simulations and simpler momentum-based methods. The validation and comparisons of the methods are made using a ducted propeller proposed by NASA. Simulations are also performed and analyzed at extended advance ratios, blade pitch setting, and cross-wind angles. Comparisons are also made with open propeller counterparts. The ducted propeller shows superior performance over its un-ducted counterpart in hover and at low advance ratios. The major thrust gain is identified from the combination of duct leading-edge suction and the higher pressure at the diffuser exit. The propeller is off-loaded due to the higher inflow velocities. The ducted propeller is also shown to have less intrusive wake features at low axial speeds. However, as the advance ratio increases, the duct thrust contribution becomes negative and the ducted propeller becomes deficient, due to growing

An earlier version of this work was presented at the AIAA SciTech Forum and Exposition, 6-10, January, 2020.

high pressure areas at the leading edge. At cross-wind, high-fidelity CFD simulations offer accurate aerodynamic loads predictions despite the complex flow features. The duct surface separation is found to be delayed due to the propeller suction, while the propeller is shown shielded by the duct, thereby suffering less from the unbalanced inflow velocities. Decomposition of induced velocities by each part is carried out and presented. A large, non-linear extra induction component, due to mutual interactions of the duct and the propeller, is observed and found favorable for the performance augmentation.

Nomenclature

Latin

AoA Angle of Attack, $^\circ$

P Pressure, Pa

V Flow Velocity, m/s

RPM Revolutions Per Minute

L Lift, N

D Drag, N

T Thrust, N

Q Torque, Nm

R Blade Radius, m

F_x Longitudinal Force, N

M_x Longitudinal Moment, Nm

M Pitching Moment, Nm

Re Reynolds Number, $Re = V_\infty c_{DF}/\nu_\infty$

c_{DF} Duct Chord, m

D_{DF} Duct Exit Diameter, m

S Area, m^2

S_{DF} Ducted Fan Reference Area, $S_{DF} = c_{DF} D_{DF}$, m^2

C_p Pressure Coefficient, $C_p = \frac{P-P_\infty}{0.5\rho_\infty (V_\infty)^2}$

C_T Propeller Thrust Coefficient, $C_T = \frac{T}{0.5\rho_\infty (V_{tip})^2 \pi R^2}$

C_l Lift Coefficient, $C_l = \frac{L}{0.5\rho_\infty (V_\infty)^2 S_{DF}}$

C_d Drag Coefficient, $C_d = \frac{D}{0.5\rho_\infty (V_\infty)^2 S_{DF}}$

C_m Pitching Moment Coefficient, $C_m = \frac{M}{0.5\rho_\infty (V_\infty)^2 S_{DF} c_{DF}}$

C_{F_x} Longitudinal Force Coefficient, $C_{F_x} = \frac{F_x}{0.5\rho_\infty (V_\infty)^2 S_{DF}}$

C_{M_x} Longitudinal Moment Coefficient,$C_{M_x} = \frac{M_x}{0.5\rho_\infty (V_\infty)^2 S_{DF} c_{DF}}$

Greek

μ Advance Ratio, $\mu = \frac{V_\infty}{V_{tip}}$

ν Kinematic Viscosity, m^2/s

η Froude Efficiency, $\eta = \frac{TV_\infty}{Q\Omega}$

Ω Rotational Speed, rad/s

Subscript and Superscript

∞ Freestream Value

tip Blade Tip Value

x Longitudinal Direction (axial direction at 0 cross-wind) Value

t Blade Tangential Direction Value

i Induced

OP Open Propeller

DF Ducted Fan

avg Azimuthal Averaged

max Azimuthal Maximum

min Azimuthal Minimum

Acronyms

AIAA American Institute of Aeronautics and Astronautics

NASA National Aeronautics and Space Administration

CFD Computational Fluid Dynamics

CAD Computational Aided Design

DFDC Ducted Fan Design Code

HMB3 Helicopter Multi-Block 3

NURBS Non-Uniform Rational B-Spline

SST Shear Stress Transport

SAS Scale Adaptive Simulation

RANS Reynolds Averaged Navier Stokes

LES Large Eddy Simulation

DES Detached Eddy Simulation

RRF Rotating Reference Frame

GCI Grid Convergence Index

I. Introduction

The ducted propeller, or ducted/shrouded fan/rotor, is a propeller enclosed in an annular duct. In hover or at low advance ratios, the duct induces higher or lower mass and momentum flow rates through the propeller disk, depending on the specific duct shape, thereby increasing or decreasing the total propulsor thrust. While higher mass flow rate is induced, the propeller blades are expected to work at higher inflow angles, hence the thrust augmentation is gained from the duct harvesting the pressure field. By shielding the propeller, the duct provides protection to ground personnel and equipment. In emergencies, the duct can support blade containment. Further, by adding guide vanes at the outlet to deflect the airflow, the ducted fan is able to provide vectorized thrust either for sideways propulsion or control purposes. Acoustic reductions can also be expected due to the duct shielding [1]. The ducted propeller has been widely used in marine propulsions [2], either to augment the thrust or to reduce tip speeds to alleviate cavitation. It has also been seen applied in ducted wind turbines [3], albeit small, to increase the efficiency. For aeronautical purposes, it has been popular for UAV/MAV/PAV (Unmanned/Micro/Personal Aerial Vehicle) applications. It is also used in compound rotorcraft as tail pusher for the Pisasecki Pathfinder, though little

information is publicized. In very recent years, due to the emerging popularity of eVTOL (Electrical Vertical Take-Off and Landing) vehicles, the ducted fan is seen as a promising choice for propulsion and lift. A detailed review of ducted fan research, including experiments, numerical simulations and optimisation, and research challenges, is presented in Reference [4].

Experimental works on ducted/shrouded propellers can be traced back to the early age of 1930s [5]. Later, many tests on ducted propulsors emerged around the 1950s [1] [6] and 1960s [7] [8] [9] [10], during the development of the 2 tilt-duct aircraft, the Bell X22 and the Doak VZ4D. Many of these tests used large or real-scale ducted fan models and provided elaborate information about geometries and test conditions. Recent experimental studies mostly focused on UAV/MAV applications [11] [12] [13]. Therefore, the model scale, compressibility, and resulting Reynolds number are only comparable to small, model-sized experiments from years ago. As suggested by Goodson and Grunwald [9], model-sized tests can be used to approximate full-scale performance, provided that the duct lip separation effects are avoided. Nevertheless, few modern tests publicised the detailed geometric definitions of their designs due to the proprietary nature or commercial reasons. Regardless, most tests confirmed the high efficiency of the ducted propeller, in hover or at low advance ratios, over the open propeller counter-part, and the thrust gain was found being from the duct. However, the ducted propeller is found to be less efficient at higher advance ratios. Few tests also examined the ducted fan performance at cross-wind conditions [8] [10] [11], which may be encountered for aircraft at very high rates of descending [10]. Apart from large changes in aerodynamic loads due to sideways flows, flow separation at the up-stream duct lip and the down-stream outer surface was also observed. However, comparing to an empty duct without the propeller, which can be taken as an annular wing [14], the stall boundary for a ducted propeller is extended due to the propeller suction [11]. Overall, due to the geometry of the duct and the blade rotation, it is hard to experimentally measure flow details inside or in close proximity to the duct. Most tests are only able to provide load balance data and are incapable of measuring the near-field pressure or velocity, especially in close proximity to the rotor. Such difficulties highlight the need for theoretical and numerical methods.

Theoretical studies and lower-order modeling of ducted fan performance using methods like the annular airfoil theory, lifting line, blade element or panel methods have been attempted since decades ago. Kriebel and Mendenhall [15] compared their theoretical analyses against experimental data, though in

many cases only qualitative agreement could be achieved. M. Drela *et al.* [16] [17] publicised a code named DFDC (Ducted Fan Design Code) based extensions of classic lifting line theory and panel methods. The code is capable of rapidly predicting the performance of ducted fans that have multiple rows of rotors and stators. More recently, Bontempo and Manna [18] studied the exact solution of incompressible, axisymmetric and inviscid flow through the duct enclosing a non-uniform actuator disk. These methods can rapidly and quite accurately predict the performance, and are suitable for fast analysis of preliminary designs. The general deficiency is that they can hardly get rid of strict assumptions, such as axial symmetry and incompressibility. In many cases, especially where flow separation is encountered, such models can only deliver results in qualitative agreement with test data, and they can hardly account for conditions like cross-wind or asymmetric duct shapes.

High-fidelity CFD (Computational Fluid Dynamics) simulations are therefore more favorable for the study of the ducted fan flows. Akturk and Camci [19] [20] [21] conducted a series of combined experimental and numerical studies on double ducted fan designs and tip clearance. They performed steady RANS (Reynolds Averaged Navier-Stokes) and the results showed good agreement with tests. URANS (Unsteady Reynolds Averaged Navier Stokes) simulations by Jimenez and Singh *et al.* [22] adopted a simplified and generalised geometry to study the ducted rotor aerodynamics. Sheng *et al.* [23] performed DES (Detached Eddy Simulation) simulations on a simplified fan-in-wing configuration. However, both studies lacked direct support from experiments. Biava and Barakos [24] applied high-fidelity URANS methods to the analysis and optimisation of a ducted propulsor for Hybrid Air Vehicles, although the data is not explicitly public. Very recently, Rubio *et al.* [25] carried out high-fidelity DDES (Delayed Detached Eddy Simulation) simulations for small-sized coaxial ducted rotors, but mostly focusing on examining solver abilities.

Overall, previous numerical studies proved that high-fidelity modeling ducted fans remains challenging due to geometries, relative motions, and complex flow features. Further, when separation appears at the duct inner or outer surface, hybrid LES/RANS formulations or scale-resolving simulations are preferred over URANS simulations. The geometry and mesh generation process is also time and effort consuming, especially for systematic or parametric studies. It is also noted that most previous simulations suffered from poor validation or very low Reynolds numbers. In addition, few considered the systematic variations

of operating conditions and their influences on the duct and propeller performance. Particularly, few to none took into account the effect of cross-wind and the associated flow features. The variation of operating conditions is significant for the assessment of ducted fan performance for further aircraft applications.

In this light, this work presents the validation and analyses of ducted propeller simulations, using different grid strategies, steady/unsteady high-fidelity CFD simulations, and lower-order predictive methods. An automatic geometry and grid generation framework is proposed and examined, in order to save time and efforts in preparing complex geometries used for ducted fans. A ducted propeller test case [8] by NASA is used for the validation. Validation is made with simulations of the empty duct at increasing AoA, of the ducted propeller in axial flight and at various cross-wind angles. Comparisons are also made the un-ducted counterpart. Assessment of ducted propeller performance for aircraft applications is then made at extended advance ratios, blade pitch angles, and several cross-wind angles. Integrated aerodynamic loads, surface pressure force vectors, wake features, propeller disk loading and induced velocities are presented and analyzed.

The present paper is organized as follows. Section II describes the numerical methods employed in the present work. Section III presents the validation results of the geometries and the methods employed against test data and lower-order methods. Also presented are the comparisons between different numerical methods and simulation strategies. Performance analyses and investigations of the ducted propeller are presented in Section IV. Last but not least, conclusions from the current study are drawn in Section V.

II. Numerical Methods

A. Automatic Grid Generation Framework

As a key part of CFD analyses and optimization, mesh generation demands a significant amount of effort and human interaction, especially for various components. To ease the effort of mesh generation and for future parametric/optimization studies, an automation framework for geometry composition and grid generation is therefore proposed and examined in the present work using the ICEM Hexa^{TM} mesher.

The ICEM Hexa^{TM} mesher is a commercial package for the generation of structured, hexahedral, and body-fitted grids. It incorporates a shell interface in Tcl/tk language with an extended library of

commands, so that automation can be realized through high-level programming. The proposed automation framework is designed to deliver not only ready-to-run, multi-block, structured grids for CFD solvers, but also geometry models for CAD tools, all from a given set of parameters. Comparing to many in-house automatic grid generation codes, the framework features a high degree of versatility and simplicity for distinct shapes. For instance, in contrast to delivering only solver-compatible grid files, grids generated using the current framework can be easily further manipulated using ICEM Hexa^{TM}. File compatibility with many modern CAE tools in terms of both input and output is also ensured.

A schematic of the current framework is presented in Figure 1. The framework is implemented using in-house codes, ICEM Hexa^{TM} scripts, and Unix shell scripts. Through in-house pre-processing codes, the input geometry is analyzed and parameterized. Features, like sectional profiles, are extracted and exported in ICEM-compatible formats. Parameters governing the geometry generation, as well as, the meshing process, e.g. outer boundary size, nodes bunching, are taken as input. Modules of the ICEM scripts are also presented in Figure 1. NURBS (Non-Uniform Rational B-Spline) based geometries are composed using the geometry module of ICEM Hexa^{TM}. The blocking process, a major part of the mesh generation that needs significant human interaction, is realized by importing pre-defined and robust mesh topologies. The design of these topologies for particular applications still needs human effort in advance, but block vertices, edges, and faces are handled by the scripts, according to the specific geometry and the parameters input. The post-processing codes convert the output to CFD solvers and external CAD tools.

The proposed framework can be easily tuned and applied to various specific shape patterns, e.g. blade/wing, fuselage, and duct/center-body for the present study. Grids are assembled using chimera overlapping strategy for the HMB3 and Fluent^{TM} simulation. The time needed for grid preparation can be reduced from hours to just a couple of minutes. This is very promising for further parametric or optimization study. Examples, evaluations, and validations of the automation tool-chain are presented in Section III. Calculations are also performed using manually generated grids for the purpose of validation and comparisons.

B. HMB3 Solver

The Helicopter Multi-Block (HMB3) [26–28] code is used in the present work. The code has been widely used in simulations of rotorcraft flows [29–32]. HMB3 solves the Unsteady Reynolds Averaged Navier-Stokes (URANS) equations in integral form using the Arbitrary Lagrangian Eulerian (ALE) formulation for time-dependent domains, which may include moving boundaries. Chimera overset grids [33] were extensively used in the current work to allow for relative motions between grids, as well as, to accommodate the automatic grid generation framework described earlier.

The Rotating Reference Frame (RRF) method is also implemented [24] for simulations with rotational periodicity, such as rotors in hover or axial flight. The HMB3 solver is enabled to solve the governing equations formulated in a non-inertial and rotating reference frame, which converts the unsteady problem into steady calculations. With the help of periodic boundaries, only a fraction of the whole computational domain is needed, thereby significantly reducing the computational cost. This strategy was adopted in the present work for simulations of ducted propellers in hover and axial flight. Similar approaches are seen often used for ducted propeller simulations by previous studies [20] [23] [24].

In the present work, most simulations were performed with the $k-\omega$ SST [34] turbulence model. The implementation has been used in previous simulations of ducted fans [24] and very good agreement with test data is achieved. For simulations of ducted fans at high cross-wind angles, when possibly excessive separation is expected, the Scale Adaptive Simulation (SAS) method [35] is used. The SAS formulation adds an additional source term to the $k-\omega$ SST equations, which allows the local adjustment of the von Karman length scale and balances contributions from the resolved and statistical components. As suggested by the DESider [36] investigation, the SAS formulations are more suitable for strongly unstable flows such as duct fans at high cross-wind angles. The SAS implementation in HMB3 has been used and validated for simulations of cavity flows [37], missile projection [38], and stall flutter [39]. Detailed assessment for propeller aerodynamic and acoustic simulations has also been carried out [40].

C. XRotor, DFDC Codes and Ansys Fluent^{TM} Solver

The XRotor and DFDC (Ducted Fan Design Codes) are open-source tools developed by Drela et.al. [16, 17, 41] for performance predicting and design of ducted/un-ducted propellers. The codes are based on extended classic blade-element/vortex theories, in combination with lifting line and panel methods. They are capable of quickly predicting, or matching the performance for specific geometries, as well as solving the inverse design problem. However, only axisymmetric conditions, e.g. hover or axial flight can be accounted for. The XRotor and DFDC codes are used in this work for comparisons with HMB3 results, as well as, to add more confidence to HMB3 results when experimental data is absent.

The general purpose solver Ansys Fluent ^{TM} solver is also used for simulations of the duct geometries (without the propeller) for comparison purposes with HMB3. Simulations using the two solvers are performed on the same grids to minimise the uncertainties, either with or without chimera/overset interfaces. Closest possible numerical settings to HMB3 are configured in Fluent ^{TM}, i.e., compressible ideal gas model, pressure far-field boundary conditions, implicit linear solver, and $k-\omega SST$ model for the turbulence modeling.

III. Numerical Validation

A. Test Matrix

To validate the HMB3 and other numerical methods, a ducted propeller test case [8] by NASA is used. The tests were carried out by Grunwald and Goodson during the early 1960s. The tested duct was a $5/16$ scaled model of the ducted propeller used on the Doak VZ-4 aircraft, but had a different propeller. Key parameters of the ducted propeller configuration and the blade shape are presented in Figures 2 and 3. Only forces and moments on the model were measured during the experiments, for variable advance ratios (at fixed RPM) and angles of attack, and also with the propeller removed. The case is chosen for its favorable model scale and Reynolds numbers over many modern tests, as well as, detailed geometric and operating definitions. Nevertheless, uncertainties are expected considering the age of the tests.

In the present work, simulations are first performed on the empty duct without the propeller at increas-

ing angles of attack, in order to verify the duct geometry, as well as, to study the duct behavior as an annular wing. Comparisons are also made against Ansys Fluent^{TM} simulations using the same grids at low angles of attack. Axial fight conditions at increasing advance ratios are then investigated using the HMB3 solver. The Reynolds number based on the duct chord and the blade tip speed is around $2.86e6$, whereas based on the tip speed and the blade tip chord it is to $2.08e5$. In the current work, the higher Reynolds number of $2.86e6$ is used and the duct chord is used as the reference length and the reference speed is the tip speed, and the flow is considered as fully turbulent. Initial simulations are also performed referring to the tip chord and speed (resulting in the lower Reynolds number), and slightly larger differences from experiments are noted. The same operating conditions are also applied to the open propeller with the duct removed. Due to the lack of detailed experimental data, the DFDC and XRotor [16, 17, 41] codes are also utilized for comparisons in axial conditions and to add more confidence in HMB3 results in the absence of experimental data . Simulations and analyses of the ducted propeller at cross-wind conditions are also carried out.

Apart from the experimental conditions for validation, off-design operating conditions, i.e. at high advance ratios and high angles of attack, are also explored and presented in the following sections to investigate the performance limitations. Detailed test conditions are listed in Table 1. The advance ratio in RRF simulations (axial cases) is changed by altering the free-stream speed, while maintaining the same blade tip speed and Reynolds number (based on tip speed and duct chord length).

B. Meshing Tool-chain Evaluation

This section presents a first evaluation of the proposed automation framework, in order to highlight its advantages in the present study. As mentioned earlier, the framework has good flexibility and versatility for different shapes and large geometric variations, e.g. blades with various sections, swept, anhedral/dihedral, and ducts with different radii, variable sections, etc. Different grid topologies are also supported. An alternative grid topology, combining the center-body/duct in the same grid, is presented in Figure 4(a). A manually generated grid with the similar topology is presented Figure 4(b). This grid is intended for the non-chimera simulations, and the results and comparisons are presented in the later section.

Note that automated grids are generated for each individual components and are to be assembled using chimera methods. This guarantees the flexibility and convenience of altering positions and combinations of components for further parametric studies. Examinations of this simulation strategy are presented in the following sections.

Details and quality comparisons of these two grids are tabulated in Table 2. The automation framework takes only about 1 minute to compose the geometry and generate the fully-structured with higher quality. It should be stated that the manually generated grid(Figure 4(b)) can be further improved, given more time and effort. The results shown here took about 8 hours, yet it needs more to reach the same quality as the automation grid. Note that for the manually generated grid, the generation of the near-field grids takes most of the time and effort. The extension of blocks to the far-field takes only a small fraction. Counting the preparation of the background grid and assembling the entire computational domain, the time need for the chimera simulation in this case is less than 30 minutes. This highlights the significant efficiency boost brought by the automation tool-chain for the present work.

Most of the grids used in this study, including background and local refinement grids, are therefore generated using the automation framework. The time needed for the pre-processing are generally reduced to minutes to hours, thus more efforts can be devoted to the simulation and analyses. Grids of different sizes are also quickly generated for the purpose of mesh independence study.

C. Validation Results and Discussions

Empty Grunwald Duct

Simulations are first performed on the empty Grunwald [8] duct at increasing pitch angles without the propeller. The tests measured aerodynamic characteristics of the bare duct with the propeller removed at increasing angles of attack. Note that the center-body shape is only approximated, as no accurate information is provided in the NASA report [8]. The rear part of the center-body is sealed with a smooth shape, as oppose to the support structures in the experiments. The impact of the accurate center-body shape is regarded as minor comparing to the duct and the propeller, but more uncertainties with respect to experiments should be expected. Especially in empty duct simulations, due to the absence of the strong

propeller influences, uncertainties brought by the approximated center-body shape may be more salient.

Topologies of the chimera grids are presented in Figure 5. The grids and geometries for the centre-body, the duct, the refinement, and the background, are all generated using the automation framework. Whereas for the non-chimera grids in Figure 4(b), geometries and grids are composed manually. Apart from numerical validation, the purpose is also to verify the effectiveness of the automation framework, and to examine if the chimera strategy is well suited for ducted fan simulations. In addition, simulations are performed at increasing cross-wind angles, in order to study the duct behaviour at cross-wind. Note that HMB3 and Fluent^{TM} can run on the output of the framework without further modifications.

A mesh convergence study for chimera simulations is carried out. Detailed descriptions of grid sizes are presented in Table 3. The mesh convergence study is carried out at $AoA = 10^{\circ}$ using grids of 3 different cell sizes and steady RANS simulations. Note that the mesh convergence study for the non-chimera grids is not included in the present paper, since most current simulations are performed using the automation framework and the chimera method. Non-chimera simulations are performed at few conditions for comparisons to verify the chimera strategy for current cases. As shown in later sections, the disagreement with chimera results is only minor, despite the differences in grids and numerical methods.

The strategy for the current chimera grid convergence study is carefully designed. It is difficult to perform grid convergence studies for complex cases such as the current one, especially when chimera grids are involved. The capability of adjusting component grids independently using chimera grids adds to the flexibility of the simulation framework, but the grid convergence study is made more complicated. Moreover, due to the hole cutting process, the actual number of cells involved in computation may vary with different grid combinations. To tackle the difficulties of the chimera grid convergence study, in the current work, cell numbers of the near-field grids, i.e. the duct and the centre-body, are progressively halved from the finest grids. Meanwhile, the background and local refinement grids, as shown in Figure 5, are kept constant with sufficient cells. This is mainly due to the fact that the chimera interpolation requires sufficient amount of cells in the background grids. Nevertheless, this strategy also ensures similar amounts of computational cells after the hole cutting in the background, for foreground grids of various cell numbers.

The calculated aerodynamic loads using the chimera grids, as well as, the finest non-chimera grid, are

presented in Table 4. The agreement between the chimera and non-chimera results is favorable, except for minor differences due to differences in grids and numerical methods such as chimera interpolations. Also, there are very small differences between the geometry used in the chimera/non-chimera grids, as the chimera geometry was composed automatically using the automation framework while the non-chimera geometry was composed manually. For the chimera results, changes in lift values are almost neglectable with respect to the grid refinement. The drag and lift-to-drag ratio predictions are changing slightly and monotonically. Lift-to-drag ratio variations over volume sizes(h^3) are plotted in Figure 6 for the 3 grid sets. In the present study, the cell size h is represented by $1/N_{cell}^{1/3}$, with N_{cell} denoting the number of cells of the grid of concern. Such a definition is a compromise yet an effective alternative, due to the complex grid topologies and geometries which make the overall cell size hard to determine. The Richardson extrapolation [42] of the current results to zero cell size yields only minor differences with the coarse grid results (within 0.6%).

The Grid Convergence Index (GCI) proposed by Roache [42] [43] is calculated using the lift-to-drag values in order to quantify the grid convergence. Detailed discussions and definitions of the GCI calculations can be found in References [42] [43]. A GCI ratio close to 1.0 indicates the grid convergence is entering the asymptotic range and further reducing the cell size will only marginally improve the result. In the current work, the refinement ratio r is defined as $\frac{h_f}{h_m}$ or $\frac{h_m}{h_c}$, where h_f, h_m, h_c are grid sizes of the fine, medium, and coarse grids as defined earlier. A constant grid refinement ratio throughout the study is ideal for the GCI calculation, while integer refinement such as grid doubling is not essentially necessary [42]. In the present study, for the near-field grids, the refinement ratio is constantly 1.26. While for the total grids, the refinement ratios are around 1.1 with slight variations.

The GCI values calculated for the 2 levels of refinement in the present study are tabulated in Table 5. With cell sizes denoted using either near-field or total grids, the GCI values are small and are decreasing with the refinement, suggesting that the relative errors are reducing with finer grids. For both cell size representations, the GCI ratio value approaches 1.0, indicating that with the current grid refinement, the grid convergence is entering the asymptotic range. Overall, the grid convergence study suggests that, using the current simulation strategy, grids of around 8 to 12 million total cells can reach the sufficient convergence for the empty duct simulation.

A further comparison is made in Figure 7 by comparing the duct and centre-body surface pressure distributions, extracted from simulations using the coarse chimera/non-chimera grids and the two CFD solvers. In general, very good correlations between solvers are observed. The agreement between different grid methods is also favourable, except that the overset simulations see more small pressure oscillations, which is noted in both HMB3 and Fluent^{TM} simulations. This may be due to the differences of geometry composition. Larger differences are mostly noted at sharp geometry transitions (diffuser exit and centre-body transitions), where the chimera grids and the Fluent^{TM} solver tend to give smoother predictions. Requirements of computational resources for the Fluent^{TM} and HMB3 steady simulations using the same baseline grid (6.6 million cells) are tabulated in Table 6. It can be seen that the HMB3 solver requires significantly lower resources over the general-purpose commercial solver in the present work.

Further steady RANS simulations ($AoA < 15°$) of the empty duct configuration are thus performed using coarse chimera grids of 6.6 million cells with both HMB3 and Ansys Fluent^{TM} simulations. The use of this coarse grid here is mainly subject to the large computational resource requirements of Fluent^{TM}. Steady HMB3 simulations using fine chimera grids of 10.2 million cells are also performed, but only minor differences are obtained, as can be expected from the previous grid refinement study. However, the fine chimera grid is used for unsteady HMB3 SAS simulations at high cross-wind angles. Lift and drag variations with increasing angles of attack are shown in Figures 8(a) and 8(b). Fluent^{TM} RANS results using the same coarse chimera grid with overset interfaces are also plotted.

Lift coefficients (Figure 8(a)) derived from the steady RANS simulations, by HMB3 and Fluent^{TM} solvers, are in favorable agreement with experimental data, until approximately $AoA > 15°$. The drag predictions (Figure 8(b)) see larger discrepancies. This can be attributed to geometric uncertainties, particularly on the approximated center-body as stated earlier. Yet the HMB3 predictions manage to predict well the trend of drag variations with respect to increasing AoA, while the Fluent^{TM} results show a different trend.

Beyond $AoA = 15°$, large differences are observed between tests and steady simulations in lift predictions. Both solvers show difficulties predicting the loads using steady methods, as large separation is expected on the up-stream inner and the down-stream outer surfaces at higher incidences. Thus unsteady SAS simulations on the fine chimera grid using HMB3 are preferred for higher cross-wind angles. SAS

simulations are not performed using Fluent^{TM}, as the SAS methods are not yet supported with the overset grid features in the employed release (2019R3). Shown in Figures 9(a) to 9(e) are iso-surfaces of non-dimensional vorticity magnitude equal to 1, indicating the shedding vortices. Non-dimensional y-vorticity contours on the middle plane (Y=0) are presented in Figures 9(b) to 9(f) for $AoA = 20°, 30°, 40°$, respectively. Flow separation arises from increasing AoA, first at the upstream diffuser exit, especially after the abrupt geometry expansion where a sudden adverse pressure gradient should be seen. As the AoA further increases, as shown in Figures 9(d) at $AoA = 30°$ and 9(f) at $AoA = 40°$, complex separation dominates the entire inner upstream surface starting from the leading edge. Large separation is also seen on the downstream outer surface. The wake of the upstream separation is also hitting the centre-body surface, creating more complex secondary flows. The 3D iso-surfaces, as shown in Figures 9(a) to 9(e), suggest low-frequency, large, hair-pin-like vortices shedding from the downstream outer surface, arising from the lip. While high-frequency, smaller vortices are seen shedding from the upstream diffuser surface. For more quantitative comparisons, as plotted in Figures 8(a) and 8(b), the aerodynamic loads are well predicted in reasonable agreement with the test data at high angles of attack, despite the large separation shown in Figures 9(a) to 9(e). Further analyses on the unsteady loads are presented in Section IV.

Ducted Propeller in Axial Flight

Simulations for the ducted propeller in axial flight in this section are performed using the Rotating Reference Frame (RRF) approach mentioned earlier. The axisymmetric, stationary walls, e.g. the duct surface, are resolved by imposing opposite rotational velocities. Note that simulations are also performed of the un-ducted propeller with the duct removed, under the same pitch and RPM settings. Details of the grid topology and numbers of points on edges of the fully-structured blade and duct grids are shown in Figures 10(a) and 10(b). A simple cylindrical grid is used for the background, with azimuthally uniform distribution, and local refinements in the vertical and radial directions for the near-field grids. Detailed comparisons, including lower-order predictions, are presented later in Section IV. Grids for each component are generated using the automation framework and assembled for calculation using the chimera approach. The total size of the ducted propeller grid is of about 12.7 million cells, for 1/3 of the complete

domain with periodic boundaries. Calculations are also conducted using the DFDC [16] [17] code for further comparisons. Validation is made at $\mu = 0.191$ in axial flight for faster convergence, which is the highest advance ratio throughout the experiments.

Results using the DFDC code [16] [17] are obtained by matching the total thrust. This results in a $\theta_{0.75}$ of 29.58° under the same RPM, free-stream speed and geometries. The same pitch setting is then applied in the CFD simulations. It should be mentioned that the blade pitch $\theta_{0.75}$ documented in the experimental report [8] is 24°. This setting was applied and examined using both DFDC and HMB3 codes, and yielded significantly lower thrust and torque. The corrected pitch setting is acquired by varying the pitch to match the total thrust using DFDC. The lower-order code solves an optimization problem minimizing the gap between the current thrust and the target value, and delivers the closest value possible. Nevertheless, the torque and the thrust contribution from each component are not constrained.

The resolved flow-fields are shown in Figures 11(a) and 11(b). The high-fidelity simulations manage to preserve clearly the tip vortices for 2 to 3 revolutions and 3 to 4 blade radii downstream the rotor disk. Figures 12(a) and 12(b) show good correlation between the methods for averaged pressure distributions along the center-body and duct. The pressure coefficients from HMB3 simulations are averaged over azimuth in order to compare with the axisymmetric results from DFDC.

Comparisons between experiments and HMB3 simulations, as well as the breakdown of propulsion forces, are listed in Table 7 and shown in Figure 13(a) and 13(b), and good agreement can be noticed between CFD, simpler predictive methods [41] [16] [17] and the test data. Note that all force and moment data are normalized using the far-field dynamic pressure, the duct chord length C_{df}, and the projected duct area S_{df}. Also presented are results for the open propeller configuration at the same pitch and RPM from HMB3 and XRotor [41]. The XRotor results are regarded as less accurate due to the lower-order nature. The purpose is to add more confidence to HMB3 results in the absence of experimental data, and the agreement between methods seen here is favorable. At this advance ratio($\mu = 0.191$) and pitch setting, the ducted and un-ducted configurations produce similar amount of total thrust, but the ducted propeller generates about 10% less torque and is hence slightly more efficient. Relative differences with respect to the experimental results are presented in Table 8. The error is defined as $[ERROR] = \frac{[prediction]-[exp]}{[exp]}$, where $[prediction]$ denotes predicted values and $[exp]$ denotes the corresponding experimental data. It

can be noted that differences between the HMB3 results and the experiments are minor in this case. The DFDC code offers fast and reasonable thrust predictions, but the torque is highly overpredicted.

Ducted Propeller at Cross-wind

Validation of the ducted propeller at cross-wind is also attempted. For these simulations, the complete computational domain and blade motions have to be used. The grid size for the ducted fan simulation is of around 16.5 million cells. Simulations of the open propeller are also performed at the cross-wind angle of 20° for comparisons. The ducted propeller simulations are performed at $AoA = 20^\circ$ and $AoA = 50\circ$ at the advance ratio of 0.191. Unsteady scale-adaptive simulations (SAS) [35] are utilized, because of the large unsteadiness and the possibly large-scale separation on the duct surface at cross-wind. The simulations adopted a time step of $1^\circ/step$. The DFDC code cannot be used in these cases as the axisymmetric assumption no longer applies.

Wake features of the ducted propeller operating at $AoA = 20^\circ$ and $AoA = 50^\circ$ are presented in Figures 14(a) to 14(c), respectively. At $AoA = 20^\circ$, the open propeller wake is preserved well by the high-fidelity HMB3 simulation. The wake is generally shifted by the free-stream, and vortices are noticed forming up behind the cylindrical center-body. The ducted propeller wake is seen less strong, but consists mostly of the blade tip vortices with slight distortion by the free-stream. It is also observed in the aerodynamic loads measurements in Figures 15(a) and 15(b) that this test point remains in the linear regime. At $AoA = 50^\circ$, complex flow features are noted as in Figure 14(c). The tip vortices are interacting with the separation flow from the duct inner surface. Separation is also observed at the downstream outer surface.

Aerodynamic load variations with increasing angles of attack are plotted in Figures 15(a) and 15(b). Note that the $AoA = 0^\circ$ data is taken from the previous steady RRF simulations. The unsteady loads are averaged over azimuth. The $AoA = 0^\circ$ data is extracted from axial flight simulations. Very good agreement with test data is seen at $AoA = 20^\circ$. At $AoA = 50^\circ$, good agreement is seen in the lift prediction, but larger discrepancies are seen in the drag and consequently the moment prediction. The current simulation at $AoA = 50^\circ$ shows reasonable agreement despite the large separation and unsteadiness, but it could perhaps be improved with finer grids and time steps, to resolve better the complex flow features

shown in Figure 14(c). In reality, however, such an extreme condition of high advance ratio and high cross-wind angle is hardly encountered for practical vehicles [10]. Hence the focus is more placed on the performance at $AoA = 20^{\circ}$. Regardless, the current predictions show good consistency with the test data.

Overall, HMB3 validation results on the empty duct and ducted propeller configurations show good agreement with test data and lower-order predictive methods. The HMB3 geometries and modeling strategies, as well as, the effectiveness of the automation framework are thus verified. The following sections present more details derived from these simulations, and focus on the performance analysis at various advance ratios, blade pitch angles, and cross-wind angles and comparisons with the open propeller counterpart.

IV. Ducted Propeller Performance Analysis

To examine the suitability of the ducted propeller as auxiliary propulsion for future compound rotorcraft, performance at various operating conditions is also investigated and discussed in this section. The advance ratio range in axial flight is extended to explore performance changes at low and high speeds. More flow details are extracted from simulations at cross-wind and analysed. Comparisons are also made against the un-ducted propeller configuration, working at the same RPM, blade pitch, and free-stream velocities. Since no open propeller tests were conducted during experiments [8], comparisons are made against XRotor [41] calculations as presented in Table 7. The aerodynamic loads from the HMB3 and XRotor codes are in good correlation with a difference of 2.6% for axial (propulsive) forces.

A. Comparisons with Un-ducted Propeller in Axial Flight

From Figures 11(a) and 11(b), it can be clearly observed that the presence of the duct significantly suppressed the extent of tip vortices. Comparisons of the axial momentum and pressure contours for the ducted/un-ducted propellers are shown in Figures 16(a) to 16(d). The presence of the duct accelerates the flow inside but slows down the wake downstream. From Table 7 and Figures 13(a) and 13(b), it can be noticed that at $\mu = 0.191$ the total thrust of the ducted propeller is only slightly higher than the open propeller. This will be shown later being the influence of the advance ratio. Regardless, the duct is found

carrying about 30% of the total thrust in the ducted propeller case. It can also be noted that the torque produced by the open propeller is higher due to the lower inflow angles. As shown in Table 9, torque contributions from the duct and the centre-body are minor. Nevertheless, the overall thrust of the ducted fan is higher, resulting in an increase in efficiency of about 0.1 comparing to the open propeller at this advance ratio, as presented in Table 7. The performance improvement is still moderate due to the advance ratio in this case, which is the highest advance ratio throughout the experiments [8].

The axial mass and momentum flow rates measured at the diffuser exit for both configurations are presented in Table 10. The presence of the duct increases both the mass and the momentum flow rates for the case calculated. The same result can be expected from simple momentum theory analyses, considering the forcedly expansion of the wake due to the diffuser exit. Further, as shown in Figures 16(a) and 16(b), the inflow is accelerated by the duct curvature at the inlet, leading to the lower regional static pressure. This causes the blades to work at higher inflow velocities and hence offloaded. Comparisons of disk loadings of the un-ducted and ducted propellers in axial flight at $\mu = 0.191$ are shown in Figures 17(a) and 17(b). The ducted rotor carries lower total thrust, with the maxima residing at the blade tip and in close proximity to the duct surface.

To further verify the contribution of the duct, the pressure coefficient distribution and surface pressure vectors at $\mu = 0.191$ are presented in Figure 18(b). It is clearly shown that the leading edge suction, and the higher pressure at the diffuser together contribute to the thrust gain of the ducted propeller. The propeller suction further decreases the pressure on the inner side of the duct, especially at the inner side leading edge before the rotor disk, where the suction forces reside. A pressure jump is caused by the rotor disk. A low pressure peak limited to a very small area can be observed due to the sudden transition of the geometry at the diffuser. The static pressure is then gradually recovered by the diffuser. Overall, the pressure forms a slightly inwards force that has a large axial component as propulsion.

Strength and features of the propulsor wake at low advance ratios are also of great interest. As future civil compound rotorcraft, serving as air taxi or air ambulance, tend to operate in close proximity to the ground. Less intrusive wakes are therefore favourable. The axial velocity magnitude measurements, extracted from the ducted and un-ducted simulations at $\mu = 0.0955$ and $\mu = 0.191$, are presented in Figures 19(a) and 19(b). The velocities are extracted from the section one duct chord length downstream

the diffuser exit, and averaged over the azimuth. The dashed lines denote the local minima and maxima at each radial station, representing the speed variations with respect to the average. The velocity profiles qualitatively agree with the wake survey by Yilmaz *et al.* [44]. As presented in Figure 19(a), the propeller wake shows a typical contraction with higher velocities concentrating in a small region. Also, larger speed variations can be noted. Whereas velocities in the ducted propeller wake are expanded and averaged over the disk, and smaller speed fluctuations are observed. When the advance ratio is increased to $\mu = 0.191$, as shown in Figure 19(b), similar features are observed, but the gap between the maximum velocities becomes smaller. In Figures 19(a) and 19(b), the vertical lines denote the averaged axial mass flux (calculated as $\frac{\oiint \rho V_x \, ds}{\oiint ds} / (\rho_\infty V_{x\infty})$) over the extraction section, normalised by the free-stream axial mass flux. Both ducted and un-ducted propellers produce higher mass flux than at the lower advance ratio of 0.0995, while the ducted propeller produces about 30% higher than the un-ducted at this low advance ratio. At $\mu = 0.191$, the ducted and un-ducted configurations produces similar mass flux magnitudes over the section, with the ducted having about 4% higher. Overall, the ducted propeller is shown to possess less intrusive and smoother wake features over its un-ducted counter part at low advance ratios for the case studied.

B. Ducted Propeller Performance at Increasing Advance Ratios and Varying Blade Pitch

As investigated by several previous experiments and calculations [24] [6] [45], the efficiency of the ducted propeller drops as the advance ratio increases. The ratio of the propeller thrust to total propulsion increases in the mean time, indicating the deficiency of the duct at high advance ratios. In this light, the advance ratio range in axial flight in this work is extended from 0.0 (hover) to 0.6447. The advance ratio is changed by changing the free-stream speed, while maintaining the same propeller RPM and blade pitch.

The thrust breakdown of HMB3 and DFDC results at increasing advance ratios is plotted in Figures 20(a) and 20(b). Experimental data is available for validation only for $\mu = 0.0$ and $\mu = 0.191$, nevertheless good correlation with HMB3 results, in terms of total thrust, propeller thrust, and duct thrust, is seen in both cases. The DFDC calculations are also in favorable agreement with HMB3 simulations, especially at lower advance ratios. Figure 20(b) shows that as the advance ratio grows, the thrust produced by each

component drops gradually and soon becomes negative. Note that at low advance ratio ($\mu < 0.1$), for the cases investigated, the duct contributes more propulsion than the propeller. However, the ratio of the duct thrust to total thrust drops quickly as the advance ratios increases, and is soon surpassed by the propeller thrust.

The same advance ratios are also applied to the un-ducted propeller using both HMB3 and XRotor calculations. The agreement is good at low advance ratios, while slight discrepancies can be seen at high advance ratios. This can be attributed to the fact that at the high advance ratios studied, the local angles of attack for the blade elements become negative and the blade mostly works near stall conditions. Due to the duct induced inflow, the ducted propeller experiences more severe stall conditions in this situation, and the difference between the DFDC and HMB3 results is hence larger. Nevertheless, the same trend can be observed for the ducted propeller calculations. While predictions for the duct force remain in good agreement at high advance ratios. The un-ducted propeller is able to produce only half of the thrust the ducted counter-part is capable of in hover. As the advance ratio increases, the un-ducted propeller thrust decreases following the similar trend as the propeller in the duct. Meanwhile, the total thrust of the ducted propeller drops faster due to the increasing duct drag, and is surpassed by the un-ducted propeller at around $\mu = 0.2$.

Comparisons of the propeller torque for ducted and un-ducted propellers are presented in Figure 21(a). The DFDC and XRotor codes generally overpredict the propeller torque, yet the predictions have the same trends as the HMB3 results. The open propeller torque increases slightly as the advance ratio increases from 0 to 0.2, then drops quickly when μ is further increased. For the ducted propeller, however, both predictions indicate that torque decreases monotonically with the advance ratio. The Froude efficiency ($\eta = \frac{TV_\infty}{Q\Omega}$) comparisons are shown in Figure 21(b). Results from different methods exhibit the same tendency and are in favorable agreement. The efficiency of the ducted propeller is higher than the open propeller by about 0.1 below $\mu = 0.2$, indicating the superior efficiency. However, the ducted propeller quickly becomes inefficient than the open propeller at high advance ratios. The negative efficiency is due to the negative thrust at $\mu = 0.382$.

To further investigate the duct thrust change at different advance ratios, the azimuthally-averaged duct surface pressure distributions from HMB3 simulations are presented in Figures 18(a) to 18(c), along with

the DFDC results for comparison. Favourable agreement between the methods is again noted at different advance ratios. The pressure force vectors on the duct surface are also extracted from HMB3 results. It is clearly shown that the duct leading edge provides a significant suction force in hover ($\mu = 0.0$). As the advance ratio increases, the pressure force on the outboard side of the leading edge gradually becomes negative. This region of negative forces grows and moves slowly inboard as the advance ratio is further increased, resulting in a net drag on the duct. As the free-stream speed grows, the pressure jump imposed by the rotor disk is no longer the dominant flow feature. The diffuser exit works regardless, but the region producing drag force is also increasing. At $\mu = 0.382$ as shown in Figure 18(c), pressure forces on the duct outer surface are not to be ignored. Contributions of pressure and viscosity are given in Figure 18(d). The major component has always been due to pressure, but the viscous part, which always contributes to the drag, also grows slightly with the advance ratio.

Overall, the duct shows higher efficiency over its open propeller counterpart, in hover or at lower advance ratios. However, the benefits diminish at higher advance ratios, with the fixed pitch and RPM, due to the duct thrust loss. In practice, however, the thrust and torque output at high speeds is often adjusted by varying the rotor RPM or the blade pitch. The RPM variation alters the advance ratio of the propulsor, besides changing the absolute velocity at the blade surface. The performance variations can be reasonably expected from previous investigations of advance ratios, as long as prominent compressibility effects does not present. It is therefore of interest to see if the ducted benefits can be retained at increased pitch angles at high speeds.

High-fidelity HMB3 simulations and lower-order calculations using XRotor and DFDC at positive and negative pitch changes relative to the original pitch setting of $\beta_{0.75} = 29.58°$ at $\mu = 0.191$ and 0.382 are performed and analysed. Larger pitch ranges are investigated using the lower-order codes due to the low computation cost. In HMB3 simulations, the pitch change is mostly implemented using RBF(Radial Basis Function) based mesh deformation. In few cases where the deformation is causing severe issues for chimera interpolation, the grids are adjusted manually with assistance of the automation framework.

Total thrust, propeller torque, and Froude efficiency variations over pitch changes at $\mu = 0.191$ and 0.382 are presented in Figures 22(a) to 24(b). The lower-order predictions of thrust by DFDC and XRotor show very favorable agreement with HMB3 results at both advance ratios. However, the torque is highly

overpredicted by the lower-order methods in both cases, comparing to HMB3 and experiments, which has also been noticed in previous investigations. This consequently leads to lower efficiency predictions. Nevertheless, the lower-order predictions and high-fidelity HMB3 calculations of torque and efficiency agree qualitatively well and are showing same trends responding to pitch variations at both advance ratios.

At $\mu = 0.191$, the ducted propeller shows a larger thrust to pitch change ratio comparing to the open configuration(Figure 22(a)). The same feature is noted in the torque results as shown in Figure 23(a). This suggests that the thrust and torque output of the ducted propeller is more sensitive to pitch changes. This can be attributed to the fact that the propeller inside the duct is subject to higher axial flow speeds due to the duct induction. The ducted propeller thrust is showing an almost linear respond to pitch variations below $+8°$, which can be expected from simple blade element analyses. The Froude efficiency (Figure 24(a)) calculated from thrust and torque results indicates the existence of an optimal pitch angle for the maximum efficiency at this speed. The optimal pitch angle for the ducted configuration is near the original setting of $29.58°$ as in the experiments, while for the open propeller the optimal angle is about $3°$ lower. Beyond or below the optimal, the efficiency drops. However, at higher pitch angles, the ducted propeller shows constantly higher efficiency over the open propeller by about 0.1, indicating the superior efficiency is maintained. The thrust-torque map at varying pitch angles is plotted in Figure 25(a). It can be seen that the ducted propeller is able to offer much higher thrust at higher pitch angles. Moreover, for the same thrust required, the ducted configuration requires much less power input at higher pitch angles and thrust, comparing to the open propeller.

At the much higher advance ratio of 0.382, favorable correlations between methods and similar responds to pitch changes are also noticed. The ducted propeller is still more sensitive to pitch variations. However, the ducted propeller generates constantly lower thrust than the open propeller (Figure 22(b)), until very high pitch increases ($> +12°$) as indicated by lower-order predications. The same is also noted in the torque results (Figure 23(b)). Existence of optimal pitch settings for maximum efficiency are also observed in Figure 24(b). Nevertheless, the open propeller efficiency is constantly higher than the ducted configuration at this high advance ratio. Regardless, it is noted that the efficiency gap between the two configurations are reducing with increasing pitch angles, although their respective efficiency values are dropping in the meantime. Extrapolations of the lower-order efficiency predictions indicate a possible

intersection point beyond $+30^{\circ}$. The thrust-torque map at varying pitch angles at this high advance ratio is presented in Figure 25(b). For the same amount of thrust require, the ducted propeller is only more efficient at very high pitch increases ($> +14^{\circ}$).

Overall, it can be concluded that the ducted propeller performance is more sensitive to pitch changes. At high advance ratios and low pitch settings, the open propeller shows better efficiency over the ducted counterpart. Nevertheless, it is shown that the superior performance of the ducted propeller can be retained at high advance ratios by increasing the blade pitch. Beyond certain, high pitch angles, the ducted propeller is able to outperform the open propeller at high advance ratios. Higher pitch angles are required at higher advance ratios. Positive correlations between the propeller thrust and the duct thrust are also noted, as shown in Figures 26(a) and 26(b). At the same axial flow speed and advance ratio of 0.191, the duct thrust is increased by 100% while the propeller thrust is increased by 40%, when the pitch is increased by $+8^{\circ}$ from the original setting as shown in Figure 26(a). In Figure 26(b) at $\mu = 0.382$, the duct axial force is recovered to positive values beyond $+8^{\circ}$ changes. It can be thus argued that the duct thrust in axial flight is determined by the relative strength of the propeller suction and the far-field velocity, rather than on the advance ratio or the absolute axial velocity. Stronger propeller suction alters the velocity and pressure fields around the duct in favor of improving the duct thrust for the case studied.

C. Ducted Propeller Performance at Cross-wind

To explore the ducted propeller performance at cross-wind, a first study is focused on the behavior of bare duct at angles of attack. It can be derived from Figure 8(a) that the empty duct itself, without the propeller, produces considerable aerodynamic loads and follows an almost linear trend with respect to AoA variations before stall. It is hence possible to use the ducted propeller for both lift generation as an annular wing [14], while still delivering propulsion. The lift slope in the linear region for the duct tested, as shown in Figure 8(a), is around 3.15, and the stall boundary is about 23°. When the propeller is installed, as shown in Figure 15(a), the lift slope approaches 5. The stall is delayed to about $AoA = 45^{\circ}$ thanks to the propeller suction [11]. The propulsion, the axial force in Figure 15(b), drops only slowly at small cross-wind angles. However, as suggested by Mort *et al.* [10], the ducted propeller is most likely

to work in axial flight or at AoA within the stall boundary.

The breakdown of aerodynamic loads on the ducted propeller at $AoA = 20^\circ$ are presented in Table 11. At the incidence of 20°, the ducted propeller generates a total force significantly higher than in the axial condition, of which the lift component is twice as much as the propulsion one. A nose-up pitching moment is also shown. In Table 11, the duct claims the most contributions to the lift and the nose-up pitching moment, while the propeller contributes the most to the forward propulsion. The center-body shows only small effects for the case analyzed. Further comparisons with the un-ducted propeller at $AoA = 20^\circ$ are tabulated in Table 12. The open propeller offers more forward thrust (C_{F_x}, and hence the Froude efficiency is slightly higher. About 40% of the total thrust contributes to the lift. While the ducted propeller produces about three times the lift, while producing 20% less thrust than the open propeller. The ducted propeller can be seen as the combination a lifting surface and a propulsor at cross-wind, and the lifting force is mostly derived from the duct. This feature can be exploited in future compound rotorcraft applications.

In order to further investigate the duct contribution, the duct surface pressure is extracted and time-averaged over revolutions, as presented in Figures 27(a) to 27(d). The surface pressure coefficient contours are presented in Figure 27(a). With the cross-wind coming from the 180° azimuth, a large region of low pressure can be noticed near the upstream (from 90° to 270° azimuth) inlet lip. The downstream lip sees generally higher pressure, as the stagnation area are moved more inboard. Sectional pressure coefficients and force vectors for the 90° and 270° azimuth are calculated and presented in Figure 27(b). The pressure distributions at these two sections are almost identical, with only small differences are seen at the inner leading-edge regions. The duct has slightly lower pressure at the rotor advancing side (90° azimuth). Large differences can be noted, however, for the 0° and 180° sections, as shown in Figures 27(c) and 27(d) respectively. The upstream section (180°) produces a large leading-edge suction on the inner surface. Whereas for the downstream section (0°), the leading-edge stagnation is moved more inboard due to the sideways flow and milder suction can be noticed on the outer surface. In this light, asymmetric geometric modifications can be made to the up- and downstream lips to accommodate local flow conditions.

D. Induction and Propeller Disk Loading at Cross-wind

Investigations on the induction and the disk loading of the ducted and un-ducted propellers at cross-wind, are also carried out and presented in this section. Comparing to the open propeller counterpart, the duct is expected to regulate the inflow and reduce inflow distortion. When installed on future compound helicopters, this is an important advantage as the propulsor may work under constant main rotor down-wash. But few to none previous experimental or numerical studies ever managed to show this feature. In addition, it is also interesting to verify the induction brought by the propeller, the duct, and their mutual interactions. The inflow profiles, the induction characteristics, and the resultant disk loading are analyzed and presented.

Thrust distributions on the propeller disk at $AoA = 0^\circ$ and 20°, for the ducted and un-ducted propellers, are presented in Figures 17(a) to 17(d). In axial flight, (Figures 17(a) and 17(b)), the open propeller experiences higher disk loading due to lower inflow ratios. High thrust loadings are seen in regions near the blade tip and slightly inboard. Whereas the ducted propeller sees lower disk loadings due to the duct induction. Also, the smaller high loading area is moved towards the blade tip and the duct surface. At $AoA = 20^\circ$, the open propeller sees higher disk loading than the ducted propeller. A large high thrust area is presented at the advancing side near the blade the tip. While for the ducted propeller, the high thrust loading is spread between azimuth 0° and 180° near the blade tip and the duct surface. Due to the duct induction, the ducted propeller is off-loaded in both axial and cross-wind conditions. At cross-wind, it is also noticed that the unbalanced disk loading is more averaged around the azimuth, but more concentrated to the blade tip. The axial force variations on the ducted and un-ducted propeller blades are shown in Figure 17(e). The un-ducted blades see higher averaged blade loadings (the dashed lines) and larger force variations.

Further investigations are made on the induction characteristics at cross-wind. The velocity $\mathbf{V}_p$ seen by the propeller blade elements can be decomposed as:

$$\mathbf{V}_p = \mathbf{V}_\infty + \mathbf{V}_{ip} + \mathbf{V}_{id} + \mathbf{V}_{ie}. \tag{1}$$

where $\mathbf{V}_\infty$ is the free-stream velocity that represents the baseline inflow condition; $\mathbf{V}_{ip}$ is the induced ve-

locity by the propeller, which can be subtracted from open propeller simulations; $\mathbf{V}_{id}$ is the duct induction, which can be subtracted from empty duct simulations; and $\mathbf{V}_{ie}$ is the extra induction by the duct/propeller combination. In this light, the axial and tangential velocity profiles at cross-wind ($AoA = 20^{\circ}, \mu = 0.191$) are extracted and analysed. Velocity data are extracted from the section $0.06R_{blade}$ upstream the rotor disk, as illustrated in Figure 28, and are decomposed into axial and tangential components. Note that the values shown are normalised by free-stream speeds, and the flow-field is time-averaged over revolutions.

This velocity decomposition approach assumes a very simple model, which considers component contributions individually and is often used in lower-order analyses such as blade element methods. Surely interference effects must be accounted for by corrections while using lower-order methods. The purpose of adopting this approach in the present study is to investigate the aerodynamic interferences between components. Similar approaches have also been seen used in interference analyses for propellers in yaw [46] and for compound rotorcraft [47]. Particularly, the term $\mathbf{V}_{ie}$ indicates the strength of the mutual interaction and highlights the importance of an accurate interaction model for lower-order methods.

The baseline tangential velocity profile by the free-stream speed, when there is a cross-wind angle of 20°, is shown in Figure 28. Tangential velocities opposite to the blade rotation are taken as positive, as illustrated in Figure 28. Subject to such a free-stream tangential speed profile, the propeller tends to generate higher thrust on the advancing side, the same as a helicopter rotor in forward flight. The axial velocity profile is the same over the propeller disk, simply as a fraction of the free-stream speed.

Induced velocity features by the empty duct are first extracted, as they represent the baseline inflow conditions the propeller inside is about to experience. The axial velocity profiles (normalized by free-stream speed) right above the rotor disk are presented in Figures 29(a) and 29(b) for incidences of 0° and 20°, respectively. Due to the induction of the duct, at $AoA = 0^{\circ}$, the propeller sees a 30% higher baseline inflow velocity for the case simulated. The radial speed distribution is almost even, with slightly higher values positioned near the duct inner surface. For the cross-wind condition (Figure 29(b)), the propeller experiences an unbalanced inflow profile.

The axial ($\mathbf{V_{ix}}$) and tangential ($\mathbf{V_{it}}$) components of the induced velocities by the duct, the propeller, and the combination, as defined in Equation 1, are presented in Figures 30(a) to 30(f). The duct induction is acquired by subtracting free-stream contributions from the empty duct simulation. At the cross-wind

angle analyzed ($AoA = 20°$), the duct induces higher axial speeds as shown in Figure 30(a). Nevertheless, the speed distribution is asymmetric stream-wise, and higher values are observed on the upstream side. The tangential induction by the duct is presented in Figure 30(b). The duct reduces the velocity on the advancing side and increases the speed on the retreating side, especially near the duct inner surface (by about 60%). This is very favorable as it eases the unbalanced flow condition experienced by the propeller at cross-wind.

The propeller induction is obtained by the subtraction of free-stream contributions from the open propeller simulation at $AoA = 20°$. The results agree qualitatively well with the study of a open propeller at yaw by Higgins *et al.* [46]. Higher axial inductions are observed mid-span near the advancing side. The maximum and minimum tangential inductions are seen near the blade root, with positive values on the advancing side. The combined induction features are in good correlation with the disk loading results shown in Figure 17(c).

The induction by the duct/propeller interference, as shown in Figures 30(e) and 30(f), is acquired by subtracting the free-stream, the duct induction, and propeller induction. The resulting velocities are due to the interaction of the duct and propeller. As shown in Figure 30(e), further higher axial inductions are observed, especially near the duct surface. This results in even higher mass flow through the propeller disk. A reduction in tangential speed on the advancing side is noted, while an increase can be seen on the retreating side. This is again favorable since it eases the unbalanced flow condition as does the duct induction. The resultant induction features of the propeller inside the duct subject to the combination of the open propeller inductions and the extra inductions. The combined propeller inductions are shown in Figures 31(a) and 31(b), and the results agree well with the disk loading features presented in Figure 17(d).

Overall, the duct induction and the flow interactions increase the axial induction through the propeller disk. The induction distributions are also altered comparing to the open propeller at cross-wind. The unbalanced tangential velocities owing to the cross-wind are eased by the duct and the propeller/duct integration. It can be concluded that the propeller inside the duct shows less unbalanced loading features at cross-wind, due to the shielding of the duct.

Conclusions

In this paper, high-fidelity CFD simulations, as well as, calculations using simpler predictive methods for ducted and un-ducted propellers are carried out and presented. A tool-chain for automatic geometry composition and grid generation is proposed and used, in order to ease efforts dedicated to the pre-processing. The numerical results are validated and compared with test data. The ducted propeller performance at various operating conditions is assessed in detail and presented. The following conclusions can thus derived from the current work:

1) Numerical methods of variable fidelity levels for ducted/un-ducted propeller simulations are evaluated and validated. High-fidelity CFD simulations of the ducted propeller test case [8] using HMB3 solver at various conditions are performed and validated. The HMB3 simulations, using different grids (chimera/non-chimera), modeling strategies (steady RRF/ unsteady mesh motions), and turbulence modeling methods, show very good agreement with experimental data, commercial solvers, and lower order-predictive methods. The maximum differences between HMB3 results and experimental data are within 4%. The HMB3 RANS and SAS modeling manages to predict the bare duct and ducted fan loads at increasing cross-wind angles. The Rotating Reference Frame implementation in HMB3 is validated and shown well-suited for ducted fan simulations in axial flight. Grid motions with chimera strategies in HMB3 are successfully applied to simulations at cross-wind. The lower-order codes, DFDC and XRotor, offer rapid and reasonable performance predictions in axial flight, but the torque is often highly overpredicted (45% off the experiments), and they cannot account for cross-wind conditions. The HMB3 solver demands significant lower computational resources (about 75% less) comparing to the commercial code Fluent ^{TM}. Overall, the HMB3 solver has shown great accuracy, efficiency, and flexibility for ducted fan simulations at various operating conditions.

2) The superior performance of the ducted propeller in hover or at low advance ratios is confirmed and investigated using numerical tools of variable fidelity levels. For the case studied, the ducted configuration produces more thrust than its un-ducted counterpart up to about $\mu = 0.2$, at the same pitch and RPM. Specially, in hover, the ducted propeller generates twice as much thrust. The Froude efficiency of

the ducted configuration is higher by about 0.1 below $\mu = 0.2$. The pitch variation study at $\mu = 0.191$ suggests that the thrust capacity of the ducted propeller studied is much higher (more than twice) than the open propeller at the same RPM. And for the same amount of thrust required, the ducted propeller requires less power input at higher pitch angles (at least 10%). The similar holds for the higher advance ratio of $\mu = 0.382$ beyond a higher pitch increase (by about $+14°$). It can be hence concluded that for the ducted propeller the duct thrust is affected by the propeller suction, while the propeller performance is determined by the duct induction which decides the inflow condition. These are further subject to conditions such as advance ratios, blade pitch, RPM, duct shapes etc. It is also noticed that the ducted propeller performance is more sensitive to pitch changes. Future investigations will be made on comparisons of the ducted/un-ducted configurations with the same propulsor radius.

3) Velocity and pressure fields of the ducted/un-ducted propellers in axial flight are investigated using high-fidelity CFD results. In axial flight, at least 25% higher mass and momentum flow rates due to the duct induction are noticed at lower advance ratios. The wake survey suggests that the ducted propeller produces less intrusive wakes while producing more thrust at low advance ratios, due to the diffuser expansion. Through the azimuth-averaged surface pressure study, the performance gain is specified as from the duct leading-edge suction and the high pressures at the diffuser. The propeller inside the duct sees a higher baseline axial velocity due to the induction of the duct, and is therefore off-loaded. However, the benefits diminishes with increasing advancing ratios. A high pressure region at the duct leading edge is found growing with increasing flight speeds, and hence reducing the duct propulsion. Nevertheless, the duct thrust and the ducted benefits are found recovering while increasing the blade pitch, which results in higher propeller suction.

4) High-fidelity CFD simulations of empty duct and the ducted propeller case at cross-wind are also performed and analyzed. The empty duct lift responses linearly to the increasing AoA before stall at around $AoA = 23°$. The stalled flows are predicted by the HMB3 SAS formulations with favorable agreement. The duct stall was delayed when the propeller is installed. Also, at $AoA = 20°$, the duct lift is found significantly augmented (twice as much), while still producing considerable thrust. This suggests that the ducted propeller can also utilized for lift generation in aircraft applications, although a nose-up

pitching moment is noticed.

5) Flow interactions and induction features of the ducted propeller are also investigated using high-fidelity CFD, and the duct shielding at cross-wind is analyzed in detail. The ducted propeller disk carries less disk loading in axial flight and at cross-wind. The disk loading is also less unbalanced at cross-wind comparing to the open propeller. High loadings are seen at the blade tip near the duct surface. Induced velocities are decomposed to identify contributions from each component and to study their interactions. Inflow features induced by the duct are favorable in terms of reducing the unbalanced flow conditions at the advancing and retreating sides. A large extra induction by the mutual interaction of the duct/propeller is noticed. This large induction significantly alters the propeller disk loading and further eases the unbalanced inflow. This feature suggests that the ducted propeller is suitable for use as propulsion for compound helicopters, working under constant main rotor downwash.

Future work needs to be continued to investigate the sensitivity of flow to geometry and carry out optimization of duct shapes to improve the high speed performance. The tip leakage flow between the blade tip and the duct surface, which affects significantly the performance, is also of interest. Coaxial ducted propellers with a second propeller row, and ducted propeller acoustics will also be evaluated.

Acknowledgments

The sponsorship of the University of Glasgow and the China Scholarship Council is gratefully acknowledged. Results were obtained using the EPCC's Cirrus HPC Service under project EC004 (https://www.epcc.ed.ac.uk/cirrus).

References

[1]Hubbard, H. H., "Sound measurements for five shrouded propellers at static conditions," Tech. rep., NACA TN-2024, 1950.

[2]Carlton, J., *Marine propellers and propulsion*, Butterworth-Heinemann, 2018.

[3]Gilbert, B., Oman, R., and Foreman, K., "Fluid dynamics of diffuser-augmented wind turbines," *Journal of Energy*, Vol. 2, No. 6, 1978, pp. 368–374.

[4]Zhang, T. and Barakos, G., "Review on Ducted Fans for Compound Rotorcraft," *The Aeronautical Journal*, Vol. 124, No. 1277, 2020, pp. 941–974.

[5]Stipa, L., "Experiments with intubed propellers," Tech. rep., NACA TM-655, 1932.

[6]Kruger, W., "On wind tunnel tests and computations concerning the problem of shrouded propellers," Tech. rep., NACA TM-1202, 1949.

[7]Grunwald, K. J. and Goodson, K. W., "Division of aerodynamic loads on a semispan tilting-ducted-propeller model in hovering and transition flight," Tech. rep., NASA TN D-1257, 1962.

[8]Grunwald, K. J. and Goodson, K. W., "Aerodynamic loads on an isolated shrouded-propeller configuration for angles of attack from -10 degrees to 110 degrees," Tech. rep., NASA TN-D-995, 1962.

[9]Goodson, K. W. and Grunwald, K. J., "Aerodynamic Characteristics of a Powered Semispan Tilting-Shrouded-Propeller VTOL Model in Hovering and Transition Flight," Tech. rep., NASA TN D-981, 1962.

[10]Mort, K. W. and Gamse, B., "A wind-tunnel investigation of a 7-foot-diameter ducted propeller," Tech. rep., NASA TN-D-4142, 1967.

[11]Martin, P. and Tung, C., "Performance and flowfield measurements on a 10-inch ducted rotor vtol uav," Tech. rep., Army Research Development and Engineering Command, Moffett Field CA, Aviation Aeroflight Dynamics Directorate, 2004.

[12]Pereira, J. L., *Hover and wind-tunnel testing of shrouded rotors for improved micro air vehicle design*, Ph.D. thesis, University of Mayland, 2008.

[13]Akturk, A., Shavalikul, A., and Camci, C., "PIV measurements and computational study of a 5-inch ducted fan for V/STOL UAV applications," *47th AIAA Aerospace Sciences Meeting including The New Horizons Forum and Aerospace Exposition*, 2008, p. 332.

[14]Fletcher, H. S., "Experimental investigation of lift, drag, and pitching moment of five annular airfoils," Tech. rep., NACA TN-4117, 1957.

[15]Kriebel, A. R. and Mendenhall, M. R., "Predicted and measured performance of two full-scale ducted propellers," Tech. rep., NASA CR-578, 1966.

[16]Youngren, H., Drela, M., and Sanders, S., "Ducted Fan Design Code," http://web.mit.edu/drela/Public/web/dfdc/, December 2005, Ducted Fan Design Code homepage, available on-line.

[17]Drela, M. and Youngre, H., "Axisymmetric Analysis and Design of Ducted Rotors," http://web.mit.edu/drela/Public/web/dfdc/DFDCtheory12-31.pdf, December 2005, Ducted Fan Design Code theory, available on-line.

[18]Bontempo, R. and Manna, M., "Solution of the flow over a non-uniform heavily loaded ducted actuator disk," *Journal of Fluid Mechanics*, Vol. 728, 2013, pp. 163–195.

[19]Akturk, A. and Camci, C., "Double Ducted Fan (DDF) as a Novel Ducted Fan Inlet Lip Separation Control Device," *the International Powered Lift Conference*, 10 2010, pp. 148–170.

[20]Akturk, A. and Camci, C., "Tip Clearance Investigation of a Ducted Fan Used in VTOL UAVS: Part 1—Baseline Experiments and Computational Validation," *ASME 2011 Turbo Expo: Turbine Technical Conference and Exposition*, American Society of Mechanical Engineers, 2011, pp. 331–344.

[21]Akturk, A. and Camci, C., "Tip Clearance Investigation of a Ducted Fan Used in VTOL UAVS: Part 2—Novel Treatments via Computational Design and Their Experimental Verification," *ASME 2011 Turbo Expo: Turbine Technical Conference and Exposition*, American Society of Mechanical Engineers, 2011, pp. 345–357.

[22]Jimenez, B. G. and Singh, R., "Effect of duct-rotor aerodynamic interactions on blade design for hover and axial flight," *53rd AIAA Aerospace Sciences Meeting*, 2015, p. 1030.

[23]Sheng, C., Zhao, Q., and Bi, N. P., "Numerical Investigations of Ducted Fan Hover Performance for FIW Applications," *53rd AIAA Aerospace Sciences Meeting*, 2015, p. 1935.

[24]Biava, M. and Barakos, G. N., "Optimisation of ducted propellers for hybrid air vehicles using high-fidelity CFD," *The Aeronautical Journal*, Vol. 120, No. 1232, 2016, pp. 1632–1657.

[25]Rubio, R. C., Diaz, P. V., and Yoon, S., "High-Fidelity Computational Analysis of Ducted and Coaxial Rotors for Urban Air Mobility," *Proceedings of the 75th Annual Forum*, Philadelphia, May 2019.

[26]Steijl, R., Barakos, G. N., and Badcock, K., "A framework for CFD analysis of helicopter rotors in hover and forward flight," *International Journal for Numerical Methods in Fluids*, Vol. 51, No. 8, 2006, pp. 819–847.

[27]Steijl, R. and Barakos, G. N., "Sliding mesh algorithm for CFD analysis of helicopter rotor-fuselage aerodynamics," *International Journal for Numerical Methods in Fluids*, Vol. 58, No. 5, 2008, pp. 527–549.

[28]Biava, M., Woodgate, M., and Barakos, G. N., "Fully implicit discrete-adjoint methods for rotorcraft applications," *AIAA Journal*, Vol. 54, No. 2, 2015, pp. 735–749.

[29]Antoniadis, A., Drikakis, D., Zhong, B., Barakos, G., Steijl, R., Biava, M., Vigevano, L., Brocklehurst, A., Boelens, O., Dietz, M., et al., "Assessment of CFD methods against experimental flow measurements for helicopter flows," *Aerospace Science and Technology*, Vol. 19, No. 1, 2012, pp. 86–100.

[30]Steijl, R. and Barakos, G., "CFD analysis of complete helicopter configurations–lessons learnt from the GOAHEAD project," *Aerospace Science and Technology*, Vol. 19, No. 1, 2012, pp. 58–71.

[31]Han, D., Pastrikakis, V., and Barakos, G. N., "Helicopter flight performance improvement by dynamic blade twist," *Aerospace Science and Technology*, Vol. 58, 2016, pp. 445–452.

[32]Garcia, A. J. and Barakos, G. N., "Numerical simulations on the ERICA tiltrotor," *Aerospace Science and Technology*, Vol. 64, 2017, pp. 171–191.

[33]Jarkowski, M., Woodgate, M., Barakos, G., and Rokicki, J., "Towards consistent hybrid overset mesh methods for rotorcraft CFD," *International Journal for Numerical Methods in Fluids*, Vol. 74, No. 8, 2014, pp. 543–576.

[34]Menter, F., "Two-Equation Eddy-Viscosity Turbulence Models for Engineering Applications," *AIAA Journal*, Vol. 32, No. 8, 1993, pp. 1598–1605.

[35]Menter, F. and Egorov, Y., "The scale-adaptive simulation method for unsteady turbulent flow predictions. Part 1: theory and model description," *Flow, Turbulence and Combustion*, Vol. 85, No. 1, 2010, pp. 113–138.

[36]Haase, W., Braza, M., and Revell, A., *DESider–A European Effort on Hybrid RANS-LES Modelling: Results of the European-Union Funded Project, 2004-2007*, Vol. 103, Springer Science & Business Media, 2009.

[37]Babu, S. V., Zografakis, G., Barakos, G. N., and Kusyumov, A., "Evaluation of scale-adaptive simulation for transonic cavity flows," *International Journal of Engineering Systems Modelling and Simulation*, Vol. 8, No. 2, 2016, pp. 106–124.

[38]Loupy, G., Barakos, G. N., and Taylor, N. J., "Multi-disciplinary simulations of stores in weapon bays using scale adaptive simulation," *Journal of Fluids and Structures*, Vol. 81, 2018, pp. 437–465.

[39]Higgins, R., Jimenez-Garcia, A., Barakos, G. N., and Bown, N., "A Time-Marching Aeroelastic Method Applied to Propeller Flutter," *AIAA Scitech 2019 Forum*, 2019, p. 1102.

[40]Chirico, G., *Aeroacoustic Simulations of Modern Propellers*, Ph.D. thesis, University of Glasgow, 2018.

[41]Drela, M. and Youngren, H., "XROTOR user guide," http://web.mit.edu/drela/Public/web/xrotor/, 2003, available on-line.

[42]Roache, P. J., "Perspective: A Method for Uniform Reporting of Grid Refinement Studies," *Journal of Fluids Engineering*, Vol. 116, No. 3, 09 1994, pp. 405–413.

[43]Roache, P. J., "Verification of Codes and Calculations," *AIAA Journal*, Vol. 36, No. 5, 1998, pp. 696–702.

[44]Yilmaz, S., Erdem, D., and Kavsaoglu, M., "Effects of duct shape on a ducted propeller performance," *51st AIAA Aerospace Sciences Meeting including the New Horizons Forum and Aerospace Exposition*, 2013, p. 803.

[45]Abrego, A. I., Bulaga, R. W., and Rutkowski, M., "Performance study of a ducted fan system," *the American Helicopter Society Aerodynamics, Acoustics, and Test and Evaluation Technical Specialists Meeting, San Francisco, CA*, 2002.

[46]Higgins, R. J., Zarev, A., Barakos, G. N., and Green, R. B., "Numerical investigation of a two-bladed propeller inflow at yaw," *Journal of Aircraft*, Vol. 57, No. 2, 2020, pp. 292–304.

[47]Öhrle, C., Schaferlein, U., Keßler, M., and Kramer, E., "Higher-order Simulations of a Compound Helicopter using Adaptive Mesh Refinement," *the AHS International 74th Annual Forum & Technology Display, Phoenix, Arizona, USA*, 2018.

List of Figures

List of Tables

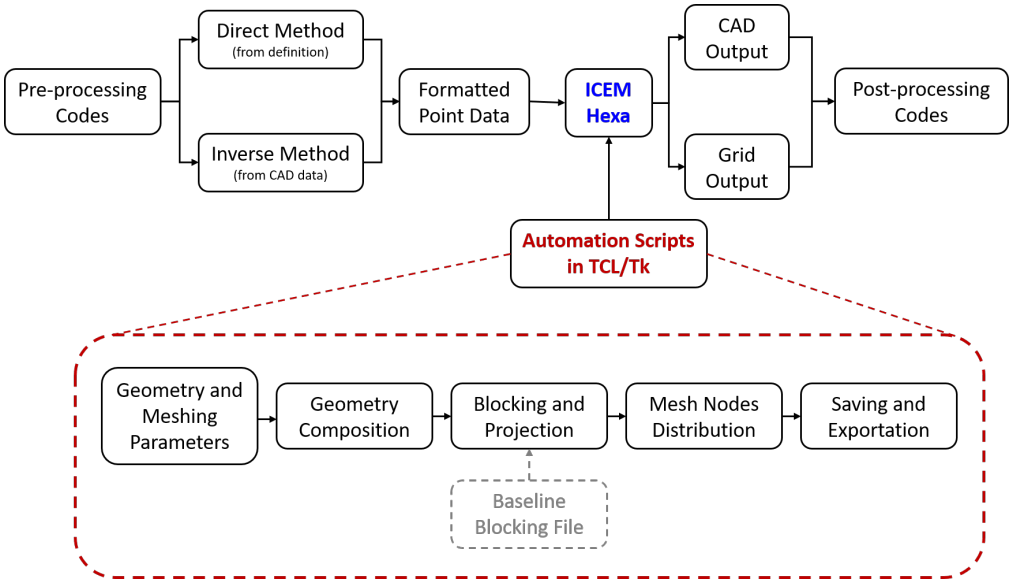

Fig. 1 Flow-chart of the automation framework for geometry composition and mesh generation.

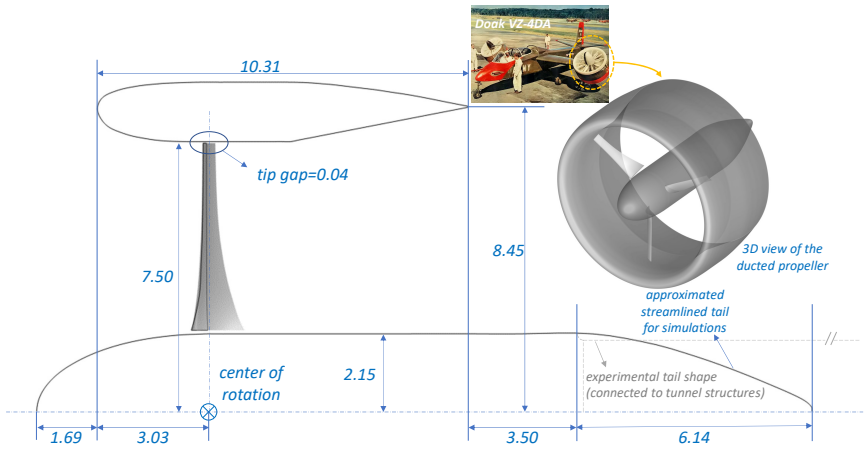

Fig. 2 Key parameters of the Grunwald ducted propeller. Details of the duct shape can be found in Ref [8]. Note the center-body tail is sealed with a streamlined shape, whereas in the experiments it is connected to tunnel structures. The ducted propeller has the same shape of the real-world design used on the Doak VZ-4D aircraft, but with a different propeller design.

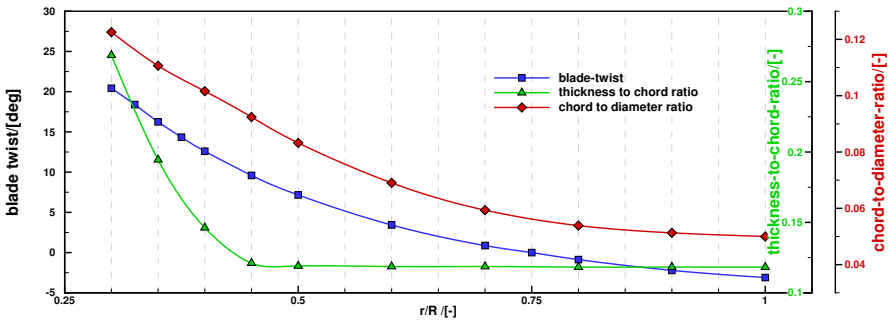

Fig. 3 Key parameters of the blade shape of the Grunwald ducted propeller [8]. Blade sections are consisted of NACA6412 shapes. The default blade pitch in the simulations is set as $\beta_{0.75} = 29.58°$, which is given by DFDC predictions, in contrast to the nominal experimental setting of $\beta_{0.75} = 24°$ [8].

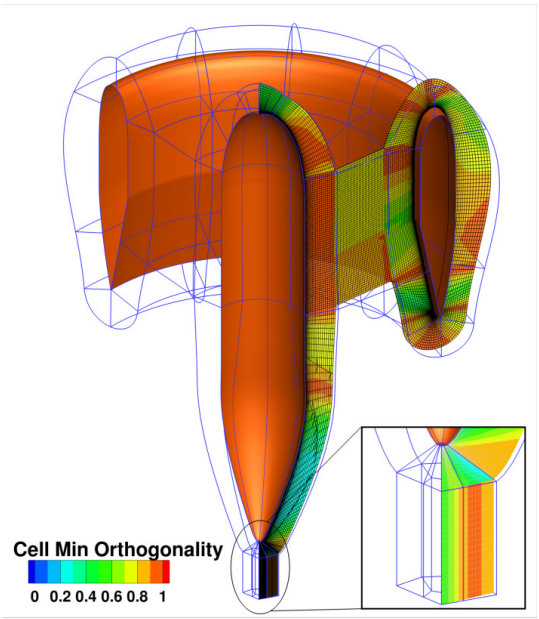

(a) Automation grid with an alternative topology combining the duct and the center-body. This grid is to be embedded in a background grid using chimera approach.

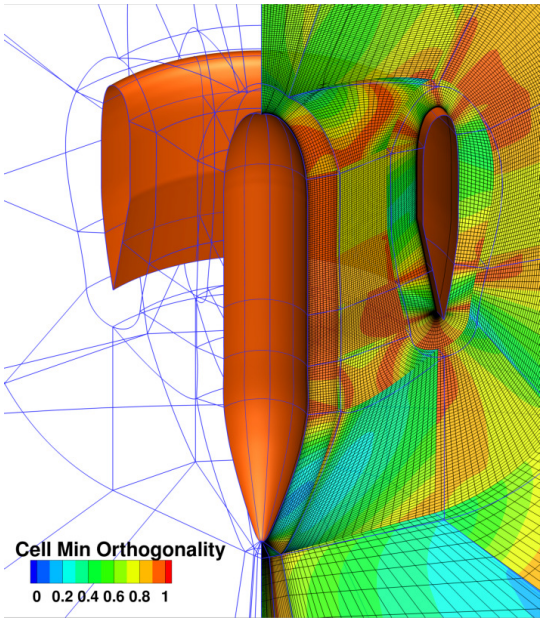

(b) Manually generated non-chimera grid for the duct and center-body.

Fig. 4 Topologies and comparisons of the automation grid and the manually generated grid. The geometry corresponds to the experiments of Grunwald and Goodson [8].

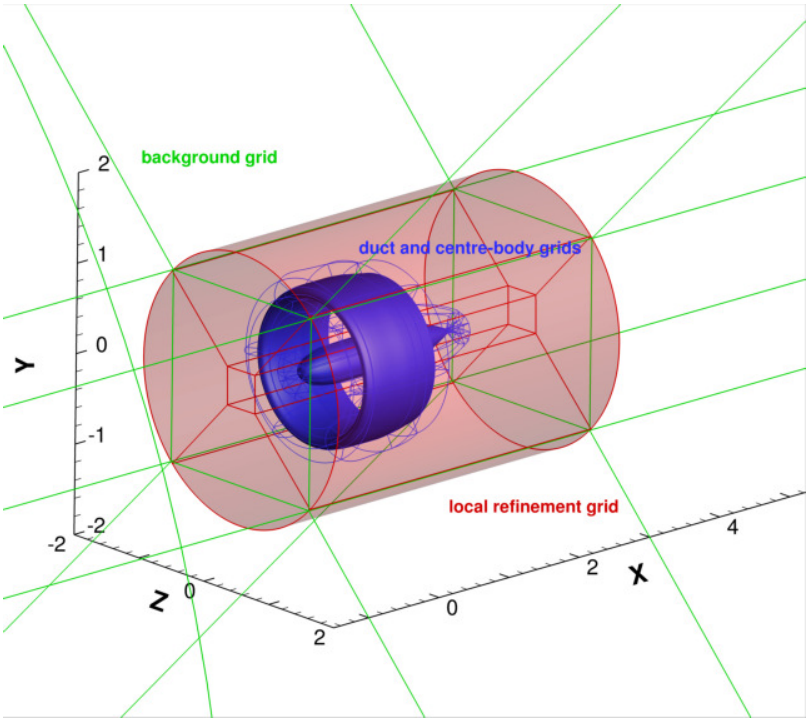

Fig. 5 Geometry and chimera grid topology of the empty duct case (generated using the automation framework).

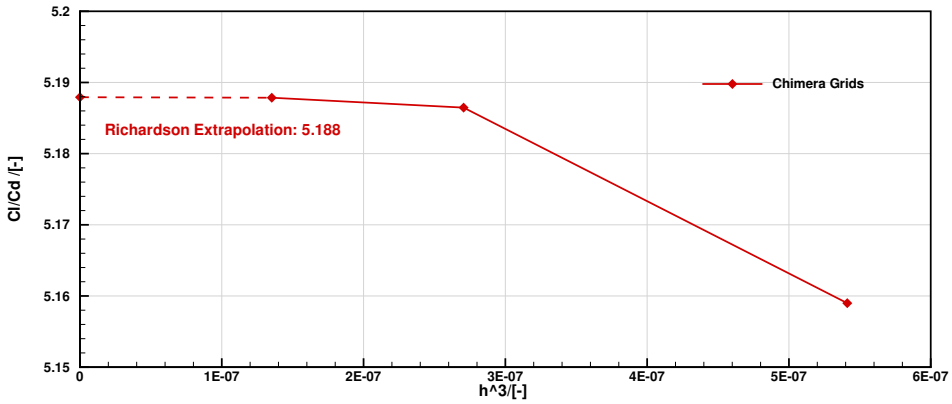

Fig. 6 Lift-to-drag variations with varing volume sizes h^3. The cell size $h = 1/N_{cell}^{1/3}$, where N_{cell} takes the sum of the near-field grid cell numbers as presented in Table 3.

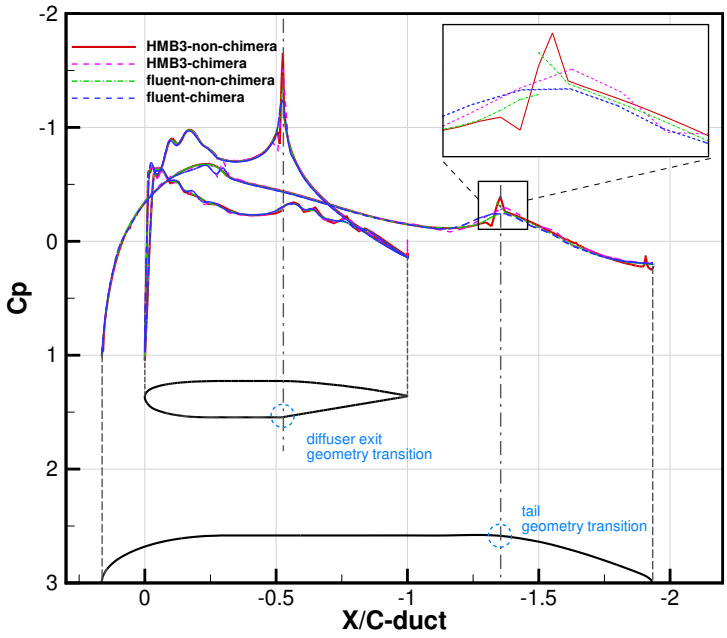

Fig. 7 Comparisons of duct and center-body surface pressure distributions extracted from HMB3 and Fluent^{TM} results, using non-chimera and overset grids.

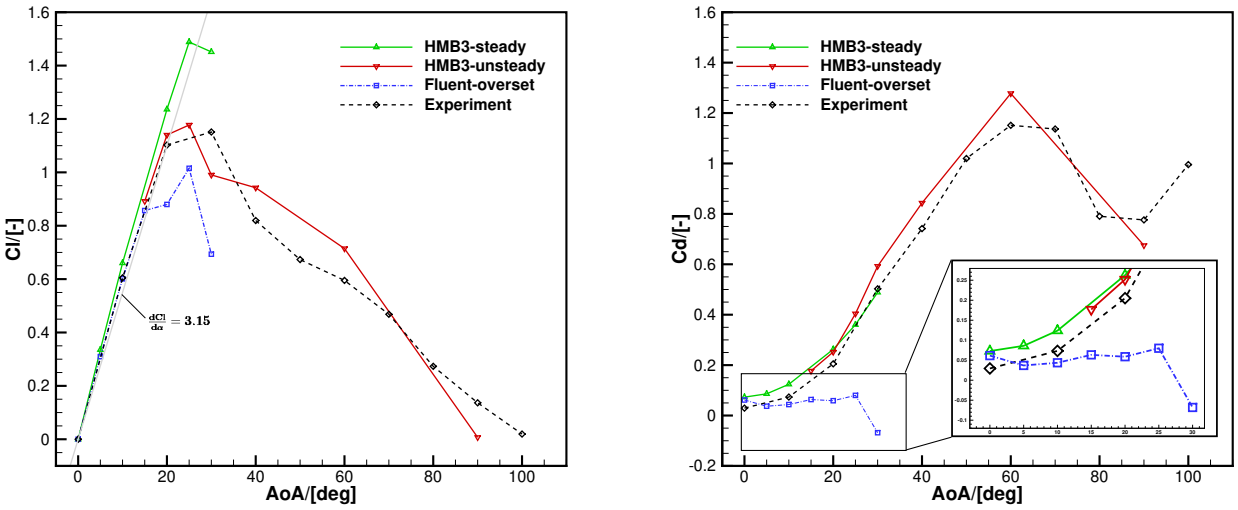

(a) Lift coefficient variations with AoA for the empty Grunwald duct.

(b) Drag coefficient variations with AoA for the empty Grunwald duct.

Fig. 8 Aerodynamic force variations with increasing AoA for the empty Grunwald duct.

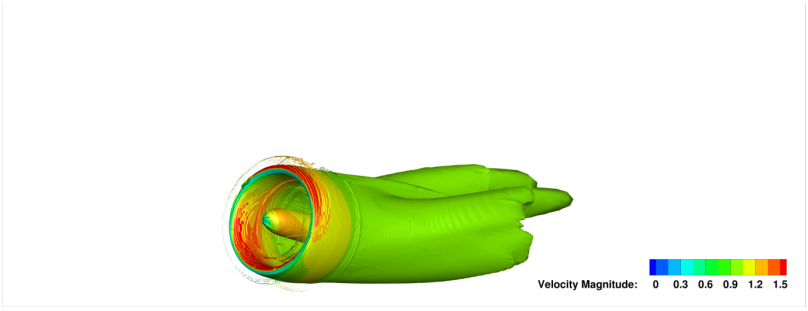

(a) Empty duct wake at $AoA = 20°$.

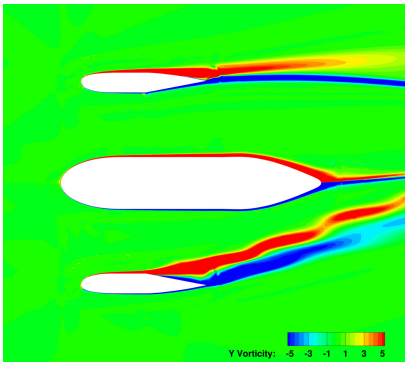

(b) Y vorticity contours at $AoA = 20°$.

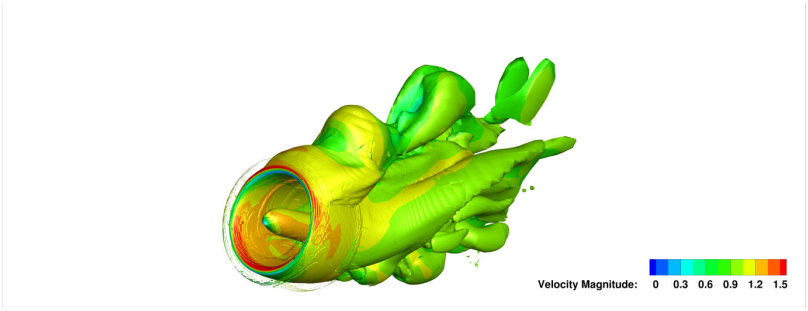

(c) Empty duct wake at $AoA = 30°$.

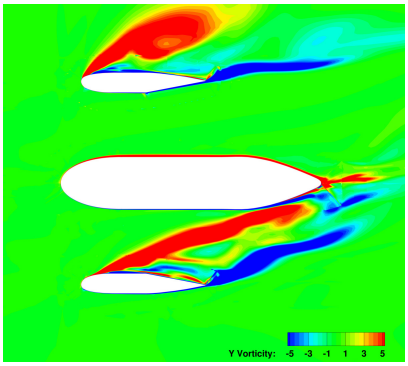

(d) Y vorticity contours at $AoA = 30°$.

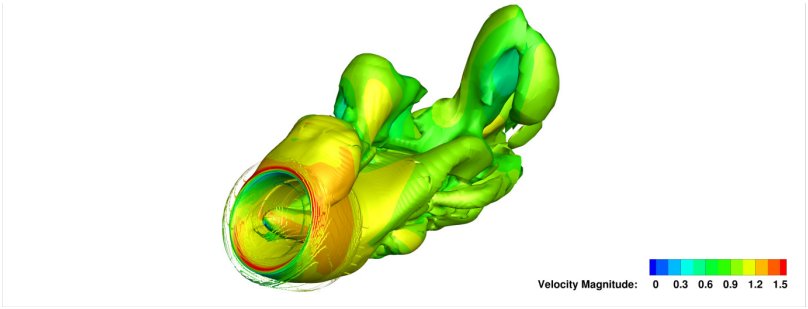

(e) Empty duct wake at $AoA = 40°$.

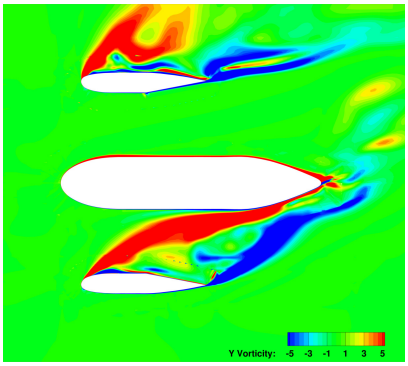

(f) Y vorticity contours at $AoA = 40°$.

Fig. 9 Iso-surfaces of non-dimensional vorticity magnitude equal to 1 for the empty duct at $AoA = 20°, 30°, 40°$, colored with non-dimensional velocity magnitude.

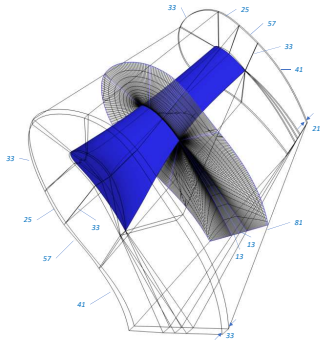

(a) Blade mesh topology and numbers of points on edges.

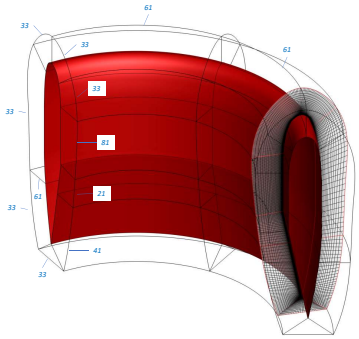

(b) Duct mesh topology and numbers of points on edges.

Fig. 10 Details of the blade and duct grids used for axial Rotating Reference Frame (RRF) simulations. The grids are copied, rotated, and merged to assemble the full configuration for unsteady simulations.

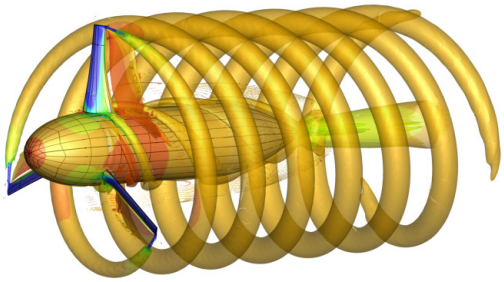

(a) Open propeller wake.

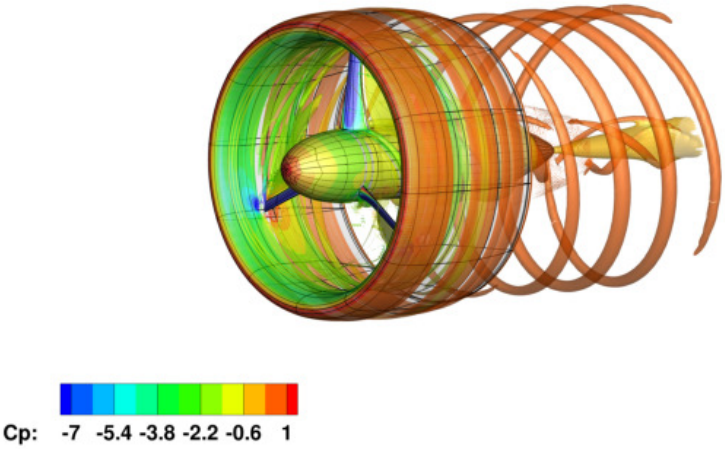

(b) Ducted propeller wake.

Fig. 11 Iso-surfaces of non-dimensional q-criterion=0.1 (normalized by blade tip speed) for the open and ducted propellers, colored with pressure coefficients.

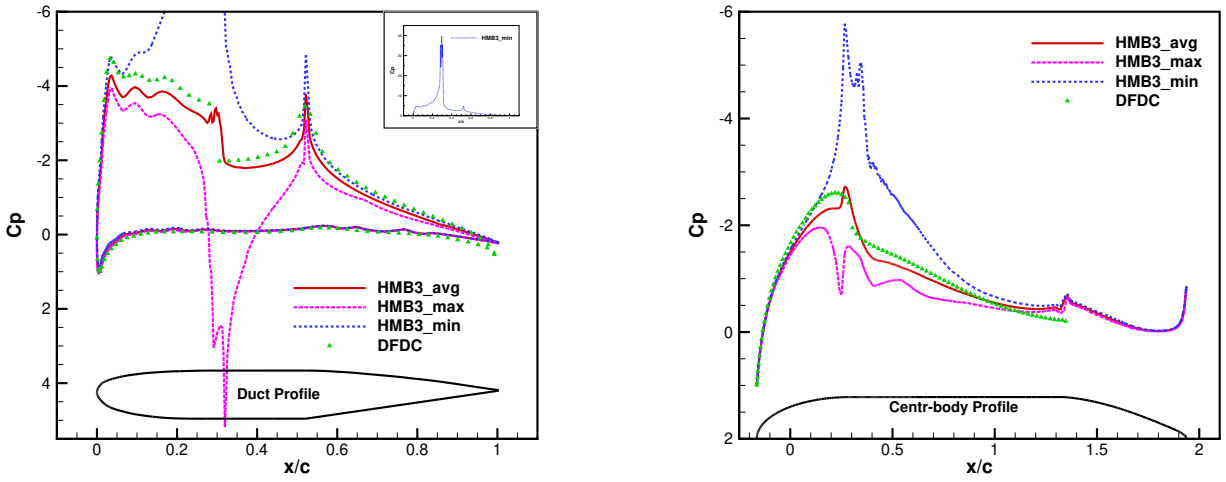

(a) Cp distribution on the duct

(b) Cp distribution on the center-body

Fig. 12 Pressure coefficient distributions along the duct and center-body surface. The peak and averaged values predicted by HMB3 are compared with the method of M. Drela [16] [17].

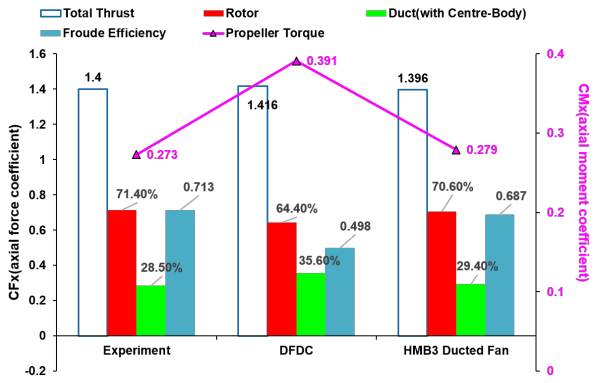

(a) Ducted propeller loads breakdown at $\mu = 0.191$ and comparisons between HMB3, experiments, and DFDC.

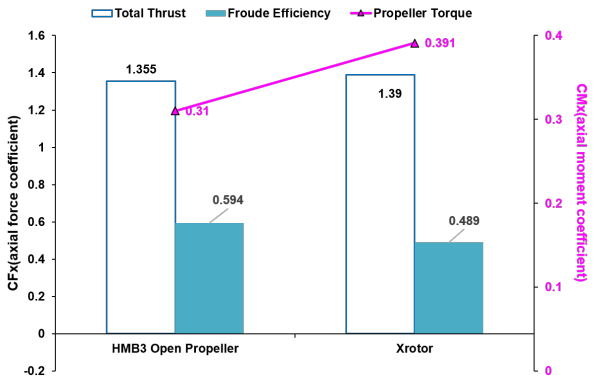

(b) Un-ducted propeller loads breakdown at $\mu = 0.191$ and comparisons between HMB3 and XRotor. The lower-order code is regarded as less accurate, yet the agreement is favorable.

Fig. 13 Aerodynamic load breakdown of the Grunwald [8] ducted/un-ducted propellers at $\mu = 0.191$ and comparisons between HMB3, experiments, and DFDC/XRotor results.

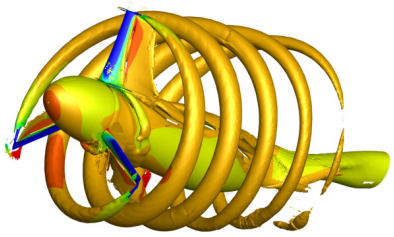

(a) Open propeller wake at $AoA = 20°$.

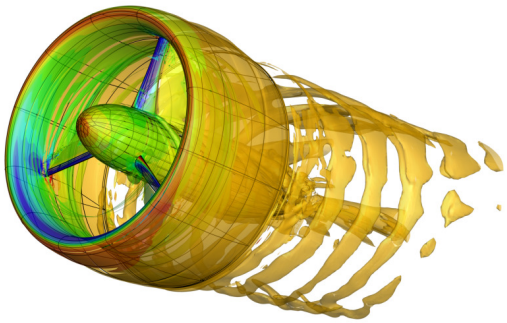

(b) Ducted propeller wake at $AoA = 20°$.

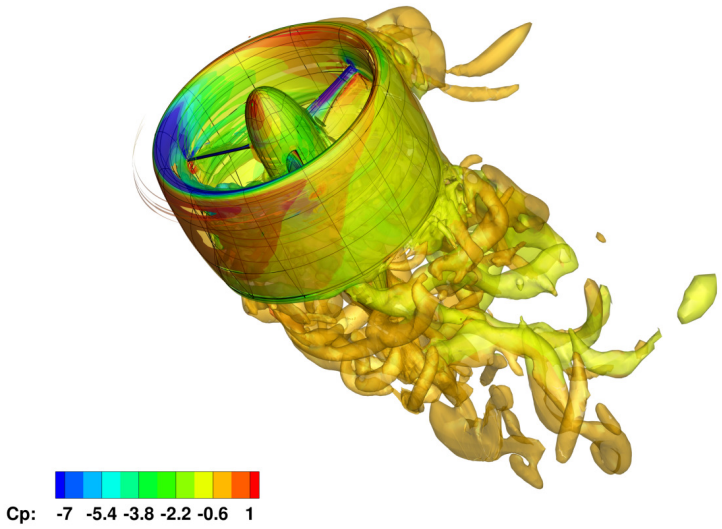

(c) Ducted propeller wake at $AoA = 50°$.

Fig. 14 Iso-surfaces of dimensionless q-criterion=5.0 (normalized by free-stream speed) for the ducted propeller at $AoA = 20°$ and $50°$, colored with pressure coefficients.

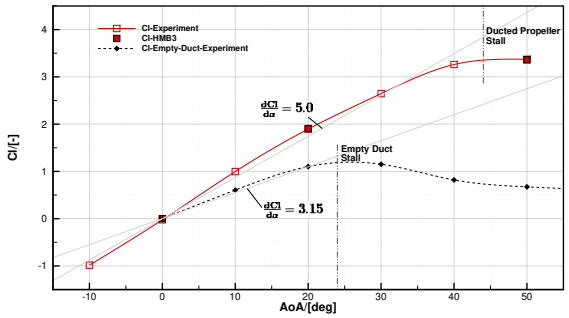

(a) Lift coeffcients of the ducted propeller at increasing AoA.

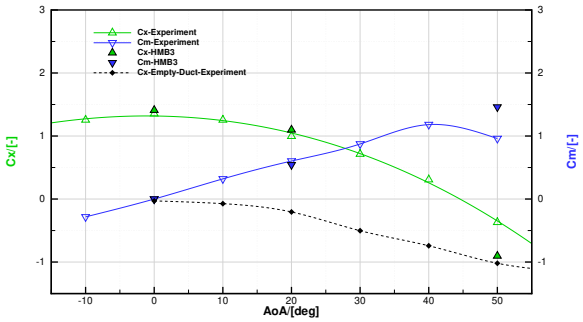

(b) Longitudinal force(drag or propulsion) and pitching moment coefficients of the ducted propeller at increasing AoA.

Fig. 15 Aerodynamic loads on the Grunwald ducted propeller working at high AoA conditions.

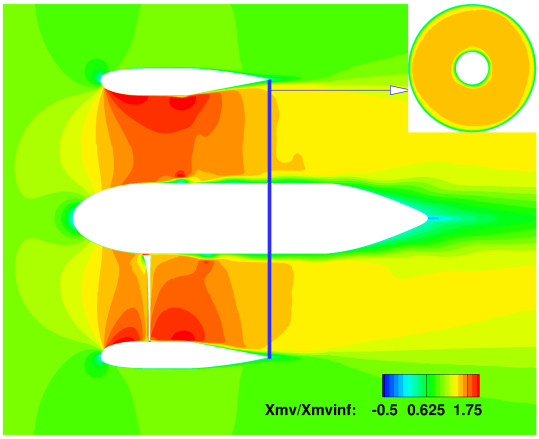

(a) Ducted propeller axial momentum.

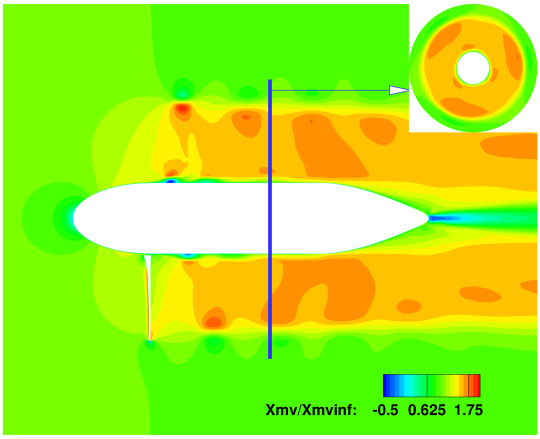

(b) Open propeller axial momentum.

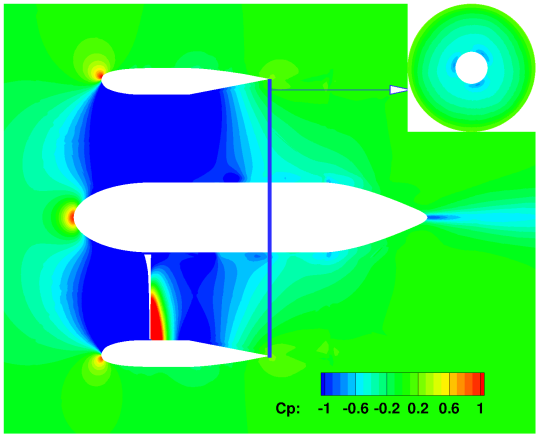

(c) Ducted propeller instantaneous pressure coefficient contours.

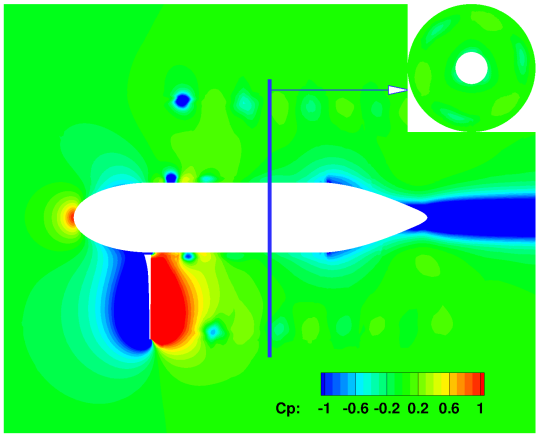

(d) Open propeller instantaneous pressure coefficient contours.

Fig. 16 Axial momentum (normalized by the far-field axial momentum) and instantaneous pressure coefficient comparisons between the ducted propeller and the open propeller ($\mu = 0.191$). Thick blue lines denote the diffuser exit sections.

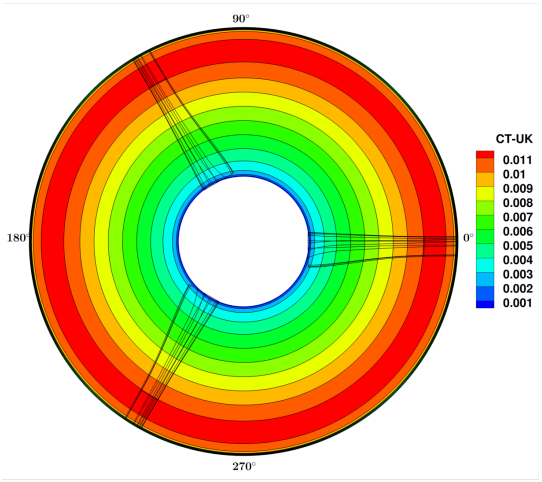

(a) Un-ducted propeller disk normal force distribution at $AoA = 0°$.

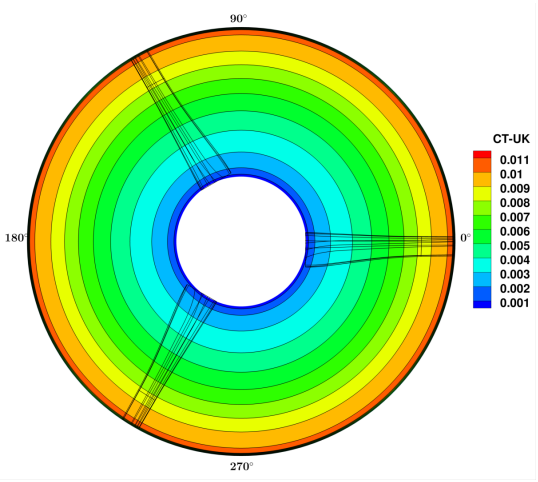

(b) Ducted propeller disk normal force distribution at $AoA = 0°$.

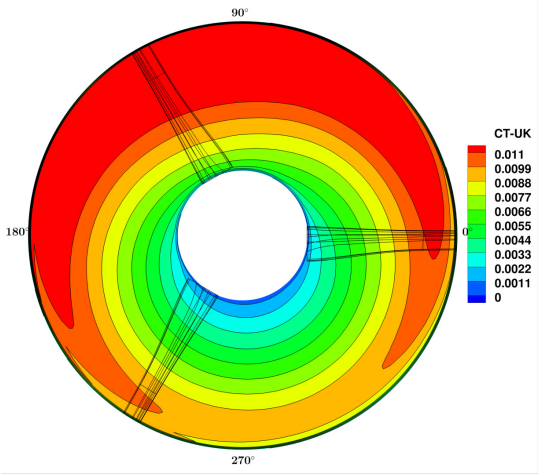

(c) Un-ducted propeller disk normal force distribution at $AoA = 20°$.

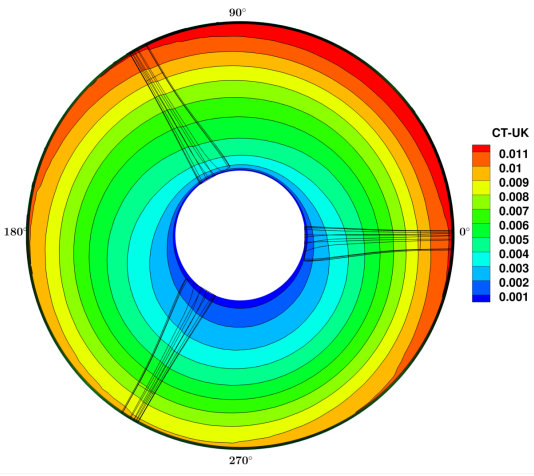

(d) Ducted propeller disk normal force distribution at $AoA = 20°$.

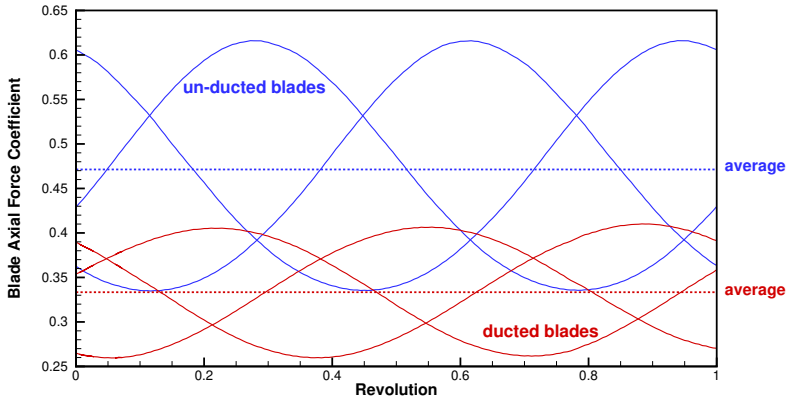

(e) Axial forces variations (including friction contributions) on the ducted and un-ducted propeller blades.

Fig. 17 Ducted and un-ducted propeller disk normal force distributions (computed using the pressure field) at $AoA = 0°$ and $AoA = 20°$.

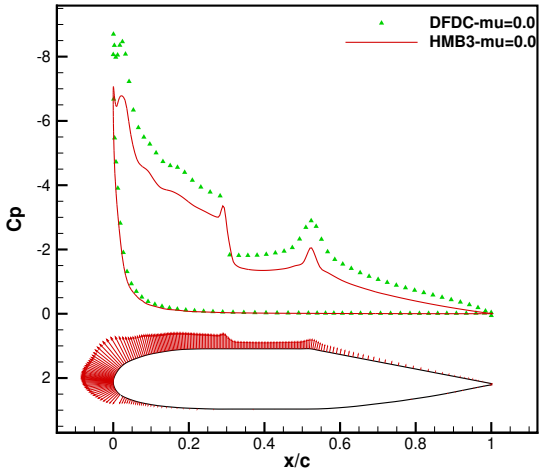

(a) Azimuth-averaged duct surface pressure distribution at $\mu = 0.0$.

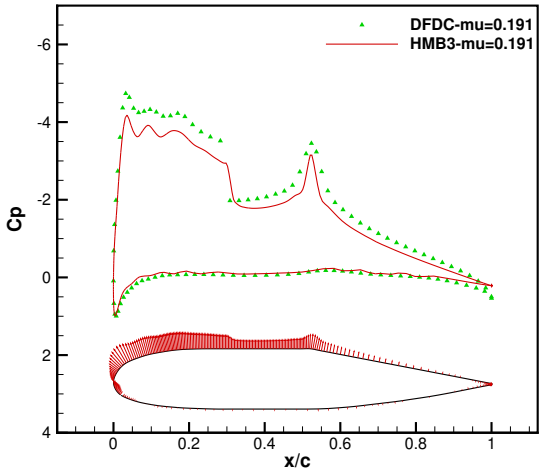

(b) Azimuth-averaged duct surface pressure distribution at $\mu = 0.191$.

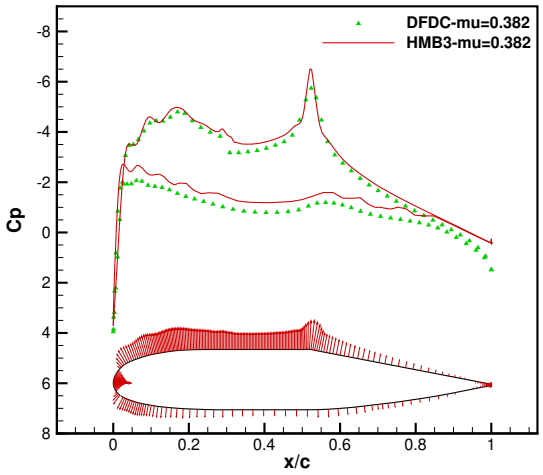

(c) Azimuth-averaged duct surface pressure distribution at $\mu = 0.382$.

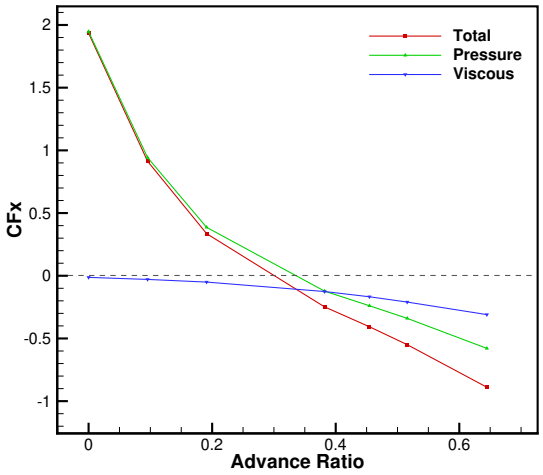

(d) Duct pressure and viscous forces breakdown at increasing advance ratios.

Fig. 18 Comparisons of duct surface pressure distributions (azimuth averaged) at low, medium, and high advance ratios, using HMB3 and DFDC calculations. Surface pressure force vectors are extracted from HMB3 simulations.

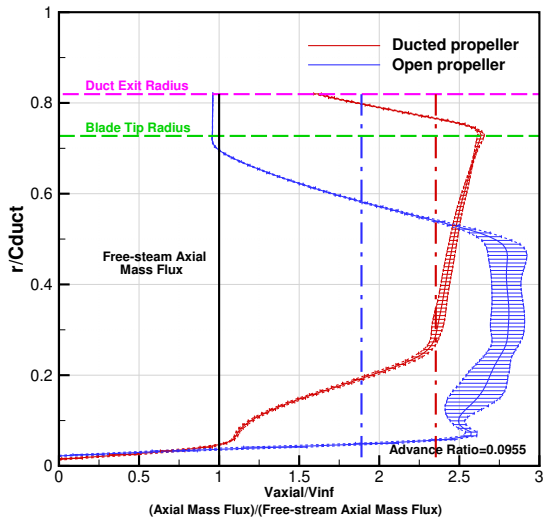

(a) Axial velocity profile comparisons of the ducted and un-ducted propellers at $\mu = 0.0955$.

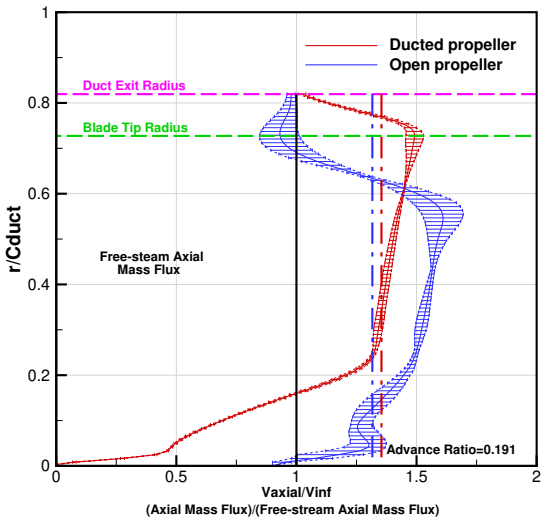

(b) Axial velocity profile comparisons of the ducted and un-ducted propellers at $\mu = 0.191$.

Fig. 19 Wake profile comparisons of the ducted and un-ducted propellers. The error bars denote the variation envelope of the velocity profile. The thick vertical lines represent the averaged axial mass flux.

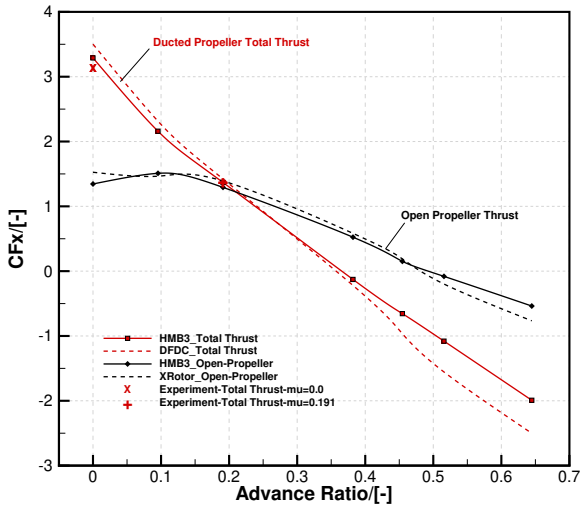

(a) Total thrust of the ducted/unducted propellers at increasing advance ratios.

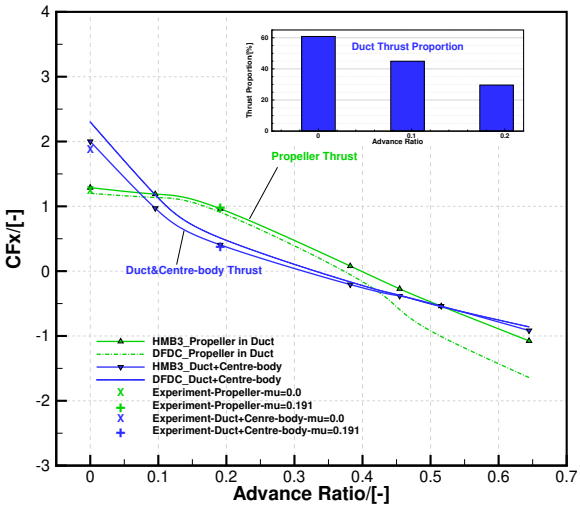

(b) Propeller and duct/center-body thrust variations at increasing advance ratios.

Fig. 20 Ducted and un-ducted propellers thrust breakdown at increasing advance ratios. All values normalized by the free-stream speed at $\mu = 0.191$ for comparison.

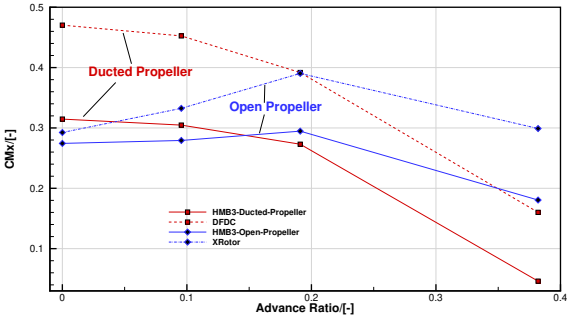

(a) Propeller axial moment (torque) variations with increasing advance ratios. All values normalized by the free-stream speed at $\mu = 0.191$ for comparison.

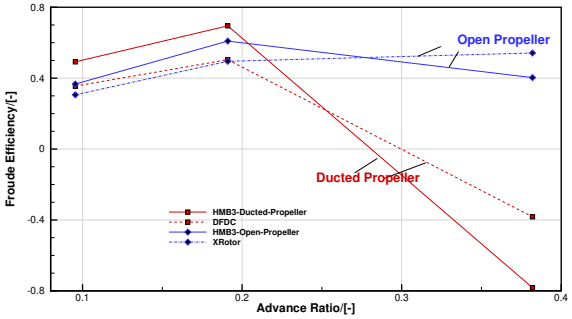

(b) Froude efficiency variations at different advance ratios.

Fig. 21 Propeller torque and Froude efficiency comparisons for the ducted and un-ducted propellers at different advance ratios.

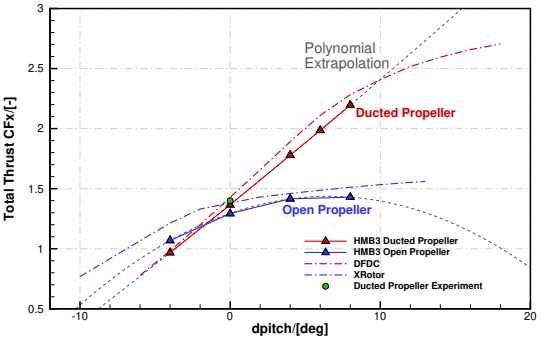

(a) Ducted/un-ducted propeller thrust variations at $\mu = 0.191$.

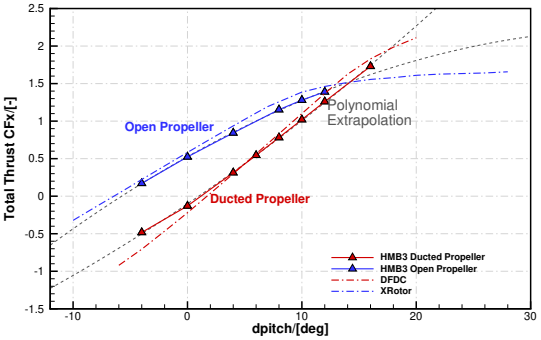

(b) Ducted/un-ducted propeller thrust variations at $\mu = 0.382$.

Fig. 22 Thrust variations with respect to pitch changes relative to $\beta_{0.75} = 29.58°$ for ducted/un-ducted propellers at $\mu = 0.191$ and $\mu = 0.382$.

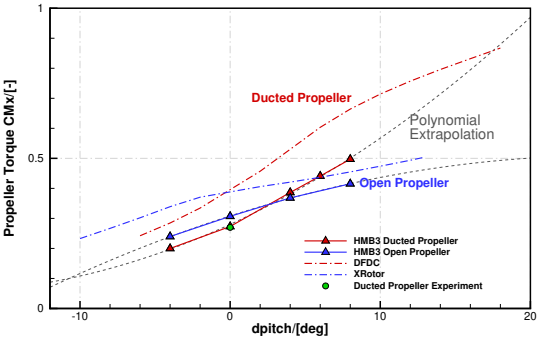

(a) Ducted/un-ducted propeller torque variations at $\mu = 0.191$.

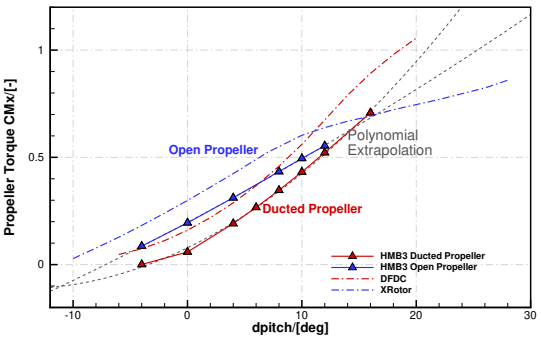

(b) Ducted/un-ducted propeller thrust variations at $\mu = 0.382$.

Fig. 23 Torque variations with respect to pitch changes relative to $\beta_{0.75} = 29.58°$ for ducted/un-ducted propellers at $\mu = 0.191$ and $\mu = 0.382$.

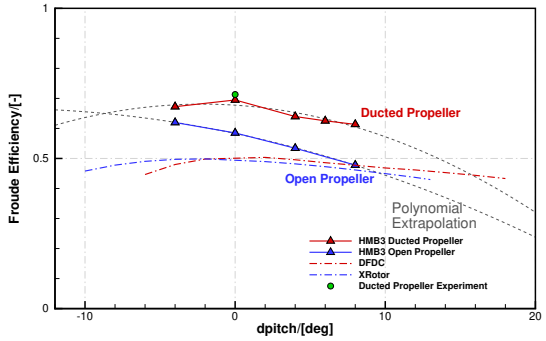

(a) Ducted/un-ducted propeller efficiency variations at $\mu = 0.191$.

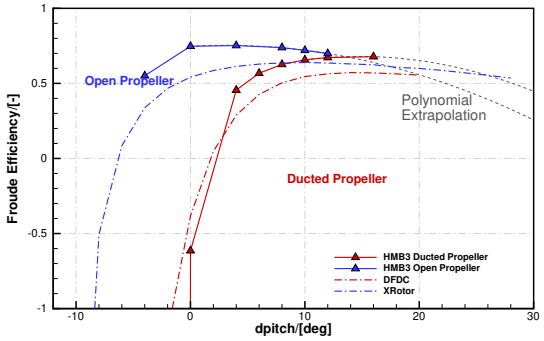

(b) Ducted/un-ducted propeller efficiency variations at $\mu = 0.382$.

Fig. 24 Froude efficiency variations with respect to pitch changes relative to $\beta_{0.75} = 29.58°$ for ducted/un-ducted propellers at $\mu = 0.191$ and $\mu = 0.382$.

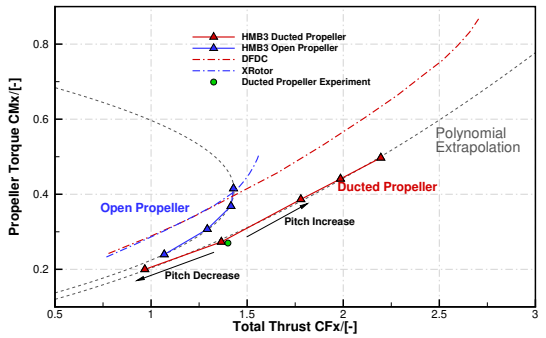

(a) Thrust-torque map over pitch changes at $\mu = 0.191$.

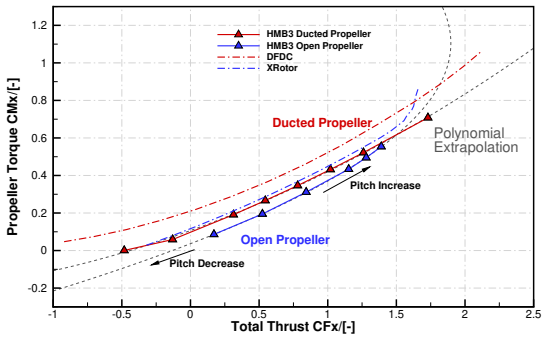

(b) Thrust-torque map over pitch changes at $\mu = 0.382$.

Fig. 25 Thrust-torque map of the ducted/un-ducted propellers with respect to pitch changes relative to $\beta_{0.75} = 29.58°$ at $\mu = 0.191$ and $\mu = 0.382$.

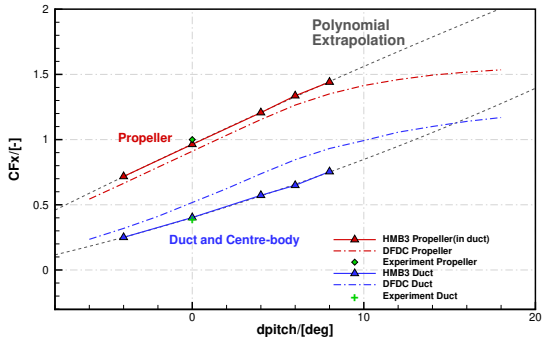

(a) Propeller and duct thrust variations at $\mu = 0.191$.

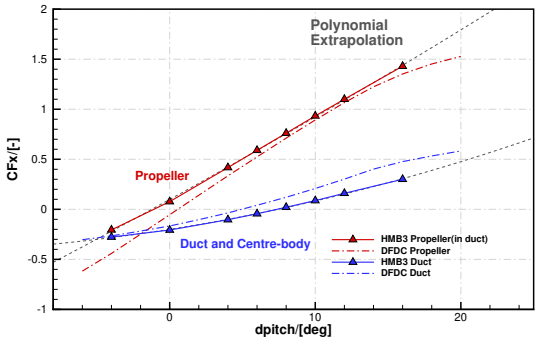

(b) Propeller and duct thrust variations at $\mu = 0.382$.

Fig. 26 Propeller and duct thrust variations of the ducted propeller with respect to pitch changes relative to $\beta_{0.75} = 29.58°$ at $\mu = 0.191$ and $\mu = 0.382$.

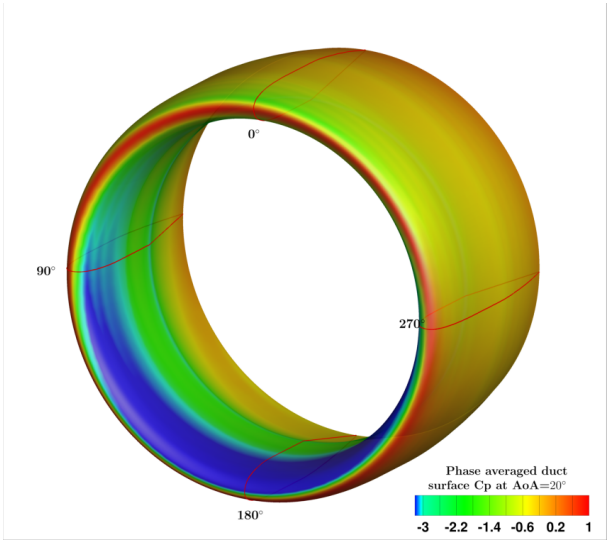

(a) Phase averaged duct surface pressure coefficient contours for the Grunwald ducted propeller at $AoA = 20°$.

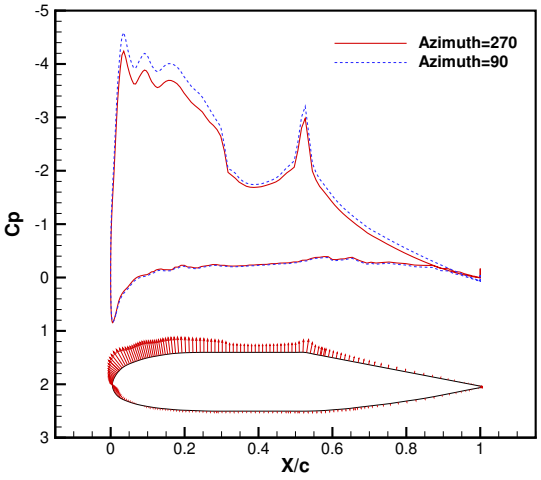

(b) Sectional pressure coefficient and vector distributions at $90°$ and $270°$ azimuth at $AoA = 20°$.

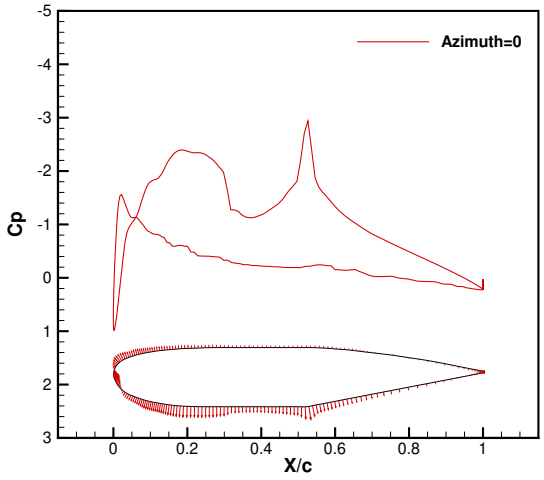

(c) Sectional pressure coefficient and vector distributions at $0°$ azimuth at $AoA = 20°$.

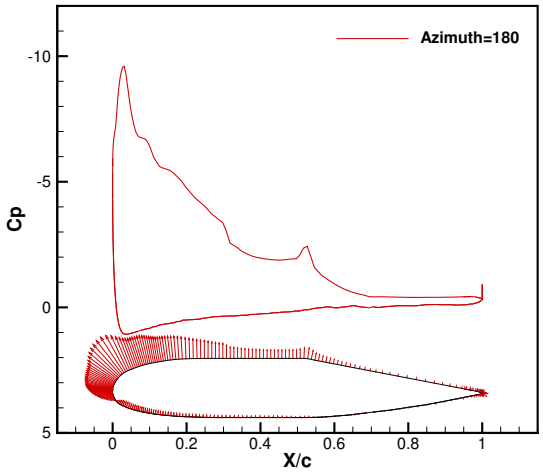

(d) Sectional pressure coefficient and vector distributions at $180°$ azimuth at $AoA = 20°$.

Fig. 27 Phase averaged duct surface Cp contours and vectors for the Grunwald [8] ducted propeller at $AoA = 20°$.

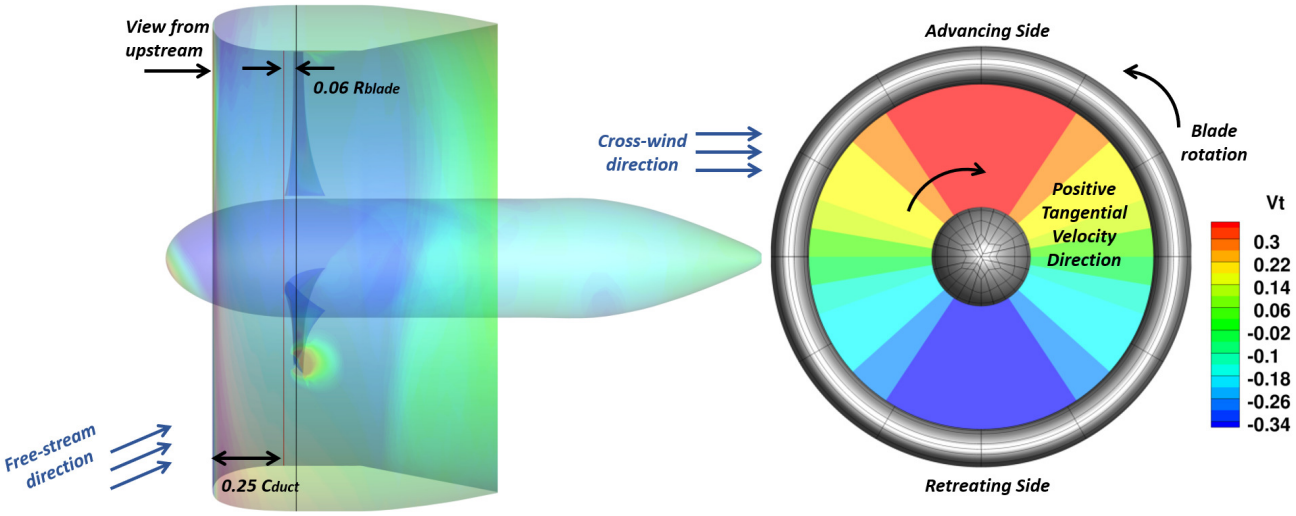

Fig. 28 Velocity extraction position and baseline tangential velocity profile due to free-stream $\mathbf{V}_\infty$ at $AoA = 20°$.

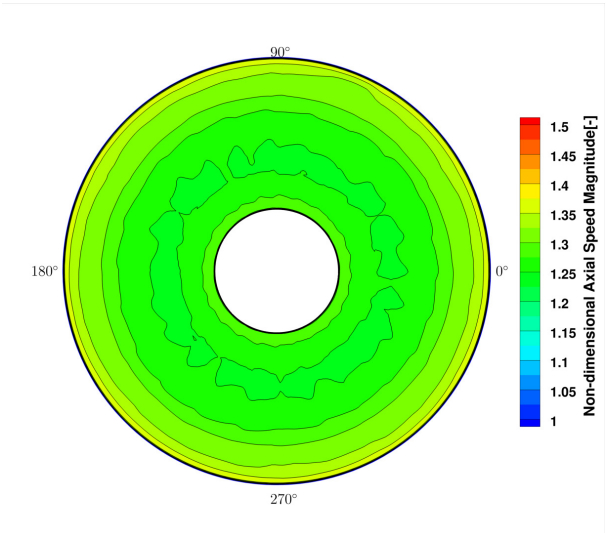

(a) Axial induction factor (normalized by free-stream speed) contours before the rotor disk of the empty duct simulation at $AoA = 0°$.

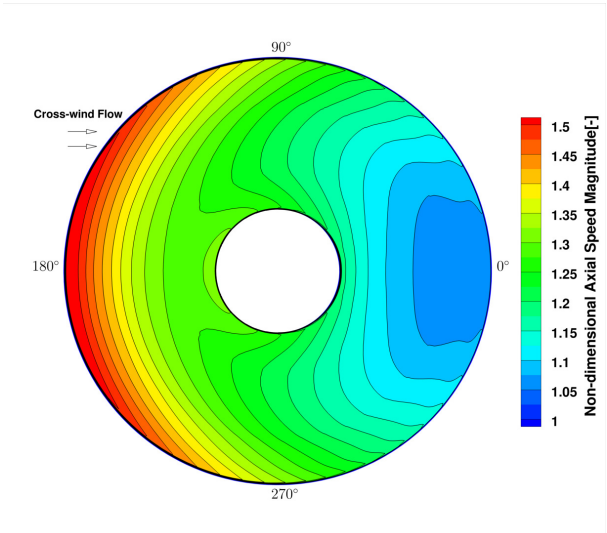

(b) Axial induction factor (normalized by free-stream speed) contours before the rotor disk of the empty duct simulation at $AoA = 20°$.

Fig. 29 Inflow velocity profiles for the rotor disk induced by the empty duct.

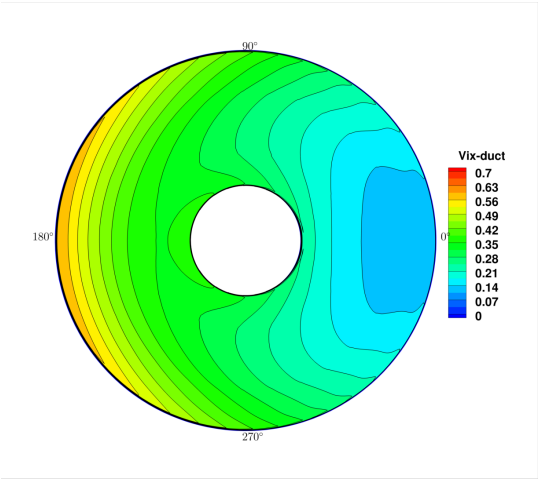

(a) Axial induced velocities by the duct, extracted from simulations of the empty duct at $AoA = 20°$.

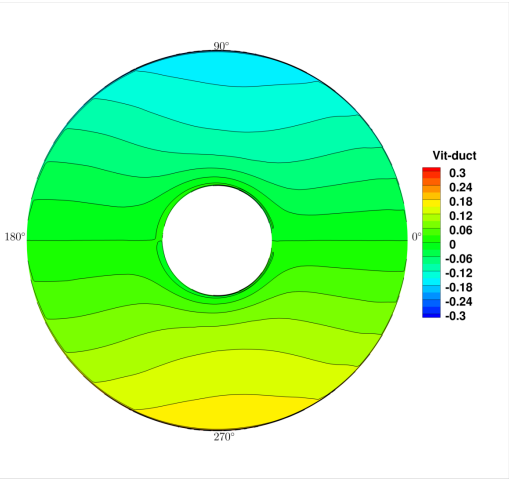

(b) Tangential induced velocities by the duct, extracted from simulations of the empty duct at $AoA = 20°$.

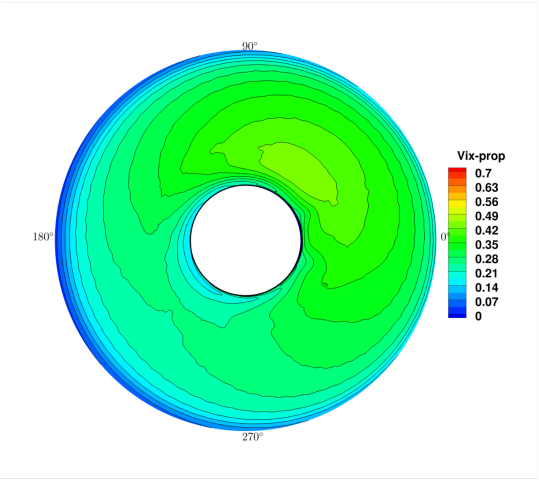

(c) Axial induced velocities by the propeller, extracted from simulations of the open propeller at $AoA = 20°$.

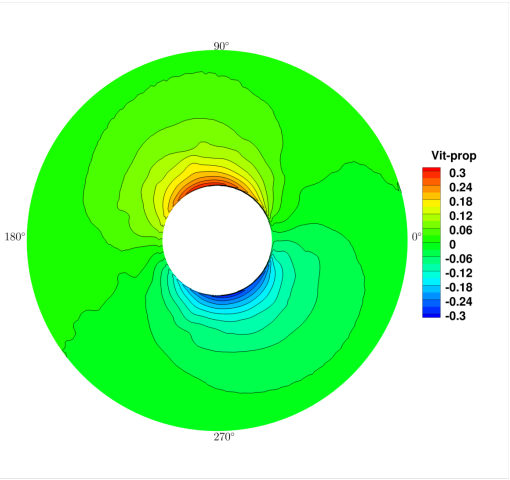

(d) Tangential induced velocities by the propeller, extracted from simulations of the open propeller at $AoA = 20°$.

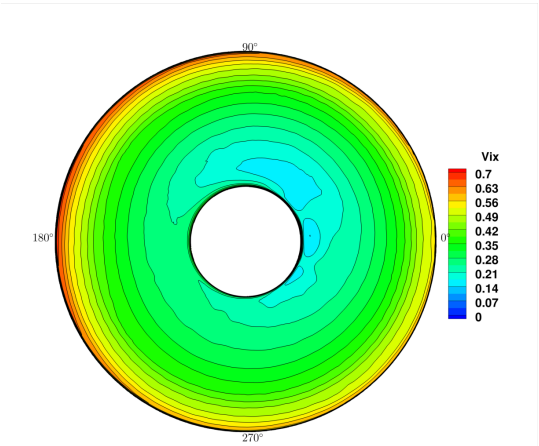

(e) Axial induced velocities by the duct/propeller combination, extracted from simulations of the ducted propeller at $AoA = 20°$.

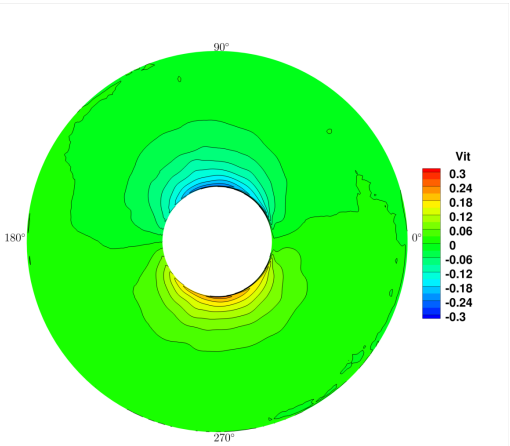

(f) Tangential induced velocities by the duct/propeller combination, extracted from simulations of the ducted propeller at $AoA = 20°$.

Fig. 30 Induced velocities by the duct, the propeller, and the duct/propeller combination, as decomposed in Equation 1.

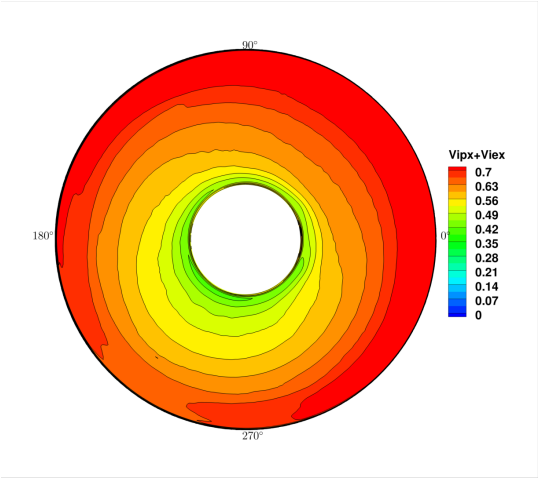

(a) Superposition of propeller axial induction and extra axial induction.

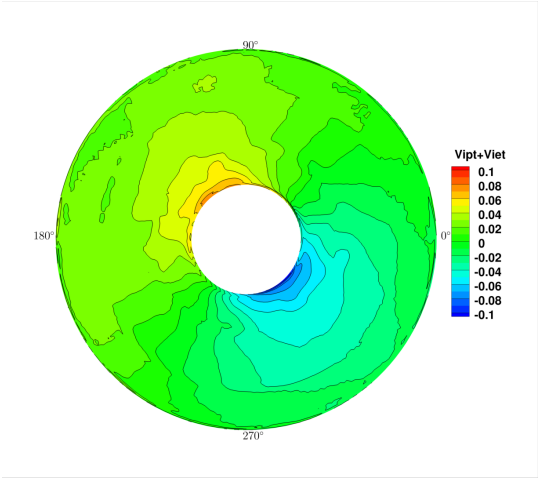

(b) Superposition of propeller tangential induction and extra tangential induction.

Fig. 31 Axial and tangential propeller induction for the Grunwald ducted propeller at $AoA = 20°$.

Table 1. Test Matrix for Ducted Fan Validation and Analysis.

Case Series	Geometry Configuration	Freestream Velocity (m/s)	Advance Ratio μ	Angle 1 (°)	Angle 2 (°)
1	Empty Duct	30.48	-	0 to 90	-
2	Ducted Propeller	30.48	0.19	0.00	20.00
3	Open Propeller	0.00-102.88	0.00-0.64	0.00	20.00
4	Ducted Propeller	0.00-102.88	0.00-0.64	0.00	-

Case Series	Angle 3 (°)	No. Blades	Tip Clearence (mm)	Rotational Speed (RPM)	Nominal Tip Mach	Purpose
1	-	-	-	-	-	Duct behaviour study
2	50.00	3	1.016	8000	0.4694	Validation and crosswind study
3	-	3	-	8000	0.4694	Comparisons with open propeller
4	-	3	1.016	8000	0.4694	Advance ratio study

Table 2. Grid quality comparisons between the automation grid and the manually generated grid. The quality criteria are evaluated using ICEM Hexa^{TM} and are all normalized ranging from 0 to 1, with 0 denoting the worst and 1 being the ideal, perfect hexahedral element.

	Grid size /[million cells]	Block Number	Min Determinant of Jacobian/[-]	Worst Distortion /[-]	Worst Skewness /[-]	Time Elapsed
Automation grid	1.9	62	0.717	0.841	0.317	$\sim$1min
Manual grid	2.7	144	0.525	0.702	0.219	$\sim$8h

Table 3. Component grid details (million cells) for the mesh convergence study of the chimera method.

Grid Size/ [Million Cells]	Background	Local Refinement	Centre-body	Duct	Near-field Total	Total
Coarse	0.74	4.38	0.77	1.08	1.85	6.97
Medium			1.54	2.16	3.70	8.81
Fine			3.08	4.31	7.39	12.51

Table 4. Aerodynamics loads comparisons of the empty duct at $AoA = 10°$ computed using the chimera grids of three different sizes and the finest non-chimera grid.

Grid Type	Grid Size	Total Cell Numbers	Lift C_l	Drag C_d	Lift-to-Drag Ratio C_l/C_d
Chimera	Coarse	6.97	0.670	0.130	5.159
	Medium	8.81	0.670	0.129	5.186
	Fine	12.51	0.670	0.129	5.188
Non-Chimera	Fine	15.26	0.641	0.126	5.084

Table 5. Grid Convergence Index (GCI) [43] calculations using the lift-to-drag ratio values with the 3 levels of grid sets in Table 3, using both near-field and overall cell size representations.

	Near-Field Grids			Overall Grids		
	Refinement Ratio	GCI	GCI Ratio	Refinement Ratio	GCI	GCI Ratio
Coarse-Medium	1.26	3.53E-04	99.97%	1.08	3.39E-04	99.97%
Medium-Fine	1.26	1.78E-05		1.12	3.76E-06	

Table 6. Computational resources comparisons between HMB3 and Ansys Fluent^{TM} using the same baseline grid.

	Grid size (cells [Million])	Memory Consumption ([GB])	CPU Time ([cores*hours])
Fluent^{TM}	6.6	∼40	∼384
HMB3	6.6	∼21	∼100

Table 7. Aerodynamic loads breakdown and comparisons between experiments, HMB3 simulations and simpler predictive methods.

C_{Fx}	EXP	Contribution	DFDC	Contribution	HMB3	Contribution	HMB3_OP	Contribution	XRotor_OP
Total	1.40	100%	1.416	100%	1.396	100%	1.355	100%	1.39
Rotor	1.00	71.4%	0.912	64.4%	0.985	70.6%	1.418	104.7%	1.39
Duct(with CB)	0.40	28.5%	0.504	35.6%	0.410	29.4%	-	-	-
Center-body	-	-	-	-	0.068	4.9%	-0.063	-4.7%	-
Propeller C_{Mx}	0.27	-	0.391	-	0.279	-	0.313	-	0.391
Efficiency η	0.713	-	0.498	-	0.687	-	0.594	-	0.489

Table 8. Relative errors with respect to the experimental data of DFDC and HMB3 predictions for the Grunwald [8] ducted propeller at $\mu = 0.191$. The relative error is defined as $[prediction] - [exp]/[exp] \times 100\%$, where $[prediction]$ is the predicted value and $[exp]$ is the corresponding experimental data.

	Total Thrust	Rotor Thrust	Duct&Center-body Thrust	Propeller Torque	Froude Efficiency
DFDC	1.14%	-8.80%	26%	44.81%	-30.15%
HMB3	-0.32%	-1.47%	2.56%	3.35%	-3.65%

Table 9. Axial moments breakdown for the Grunwald [8] ducted fan and the open propeller at $\mu = 0.191$.

C_{Mx}	HMB3$_{df}$	Contribution	HMB3$_{op}$	Contribution
Total	0.282	100%	0.314	100%
Rotor	0.279	99.07%	0.313	99.8%
Duct	0.0027	0.96%	-	-

Table 10. Axial mass and momentum flow rates measured in HMB3 simulations for the ducted and un-ducted propellers at $\mu = 0.191$, integrated over the diffuser exit section (see Figures 16(a)).

Configuration	Axial mass flow rate $\dot{m}$	Axial momentum flow rate $\dot{m}u$
Open propeller	1.363	1.946
Ducted fan	1.439	2.139

Table 11. Aerodynamic load breakdown for the Grunwald ducted propeller [8] at $AoA = 20°$.

	C_l	Contribution	C_{F_x}	Contribution	C_m(pitching)	Contribution
Total	1.922	-	1.096	-	0.504	-
Duct	1.483	77.17%	0.120	10.96%	0.440	87.32%
Propeller	0.405	21.09%	0.923	84.25%	0.064	12.68%

Table 12. Comparisons of aerodynamic loads of the ducted and un-ducted propellers at $AoA = 20°$.

	C_l	C_{F_x}	Propeller C_T	Propeller C_Q	Froude Efficiency η
Ducted Propeller	1.922	1.096	0.037	0.014	0.534
Open Propeller	0.603	1.259	0.050	0.015	0.570